

Measuring Tissue Stiffness Using Ultrasound

by

Matthew Graham (JE)

Fourth-year undergraduate project

in Group F, 2011/2012

I hereby declare that, except where specifically indicated, the work submitted herein is  
my own original work.

Signed: \_\_\_\_\_ Date: \_\_\_\_\_

# CONTENTS

<b>1</b>	<b>Introduction</b>	<b>3</b>
1.1	Problem overview . . . . .	3
1.2	Elastography fundamentals . . . . .	3
1.2.1	Imaging modality . . . . .	3
1.2.2	Tissue excitation method . . . . .	4
1.3	Review of relevant existing techniques . . . . .	5
1.3.1	Window similarity based displacement estimation . . . . .	5
1.3.2	Quasi-static ultrasound elastography . . . . .	6
1.3.3	Dynamic ultrasound elastography . . . . .	6
1.4	Project motivation and aims . . . . .	8
<b>2</b>	<b>Theory</b>	<b>10</b>
2.1	Tissue mechanical model . . . . .	10
2.1.1	Assumptions . . . . .	10
2.1.2	Governing equation . . . . .	11
2.2	Inversion based methods . . . . .	12
2.3	Arrival time based methods . . . . .	13
2.4	Finite difference simulation . . . . .	14
<b>3</b>	<b>Development of Method</b>	<b>15</b>
3.1	Displacement measurement . . . . .	15
3.1.1	Scan sequence choice . . . . .	15
3.1.2	Implementation details . . . . .	18
3.2	Shear wave generation . . . . .	19
3.2.1	Initial phantom tests . . . . .	19
3.2.2	Effect of probe motion . . . . .	23
3.2.3	Effects of rigid boundaries of phantom . . . . .	25
3.3	Shear modulus estimation . . . . .	27
3.3.1	Arrival time based methods . . . . .	28
3.3.2	Direct inversion . . . . .	30
<b>4</b>	<b>Results and Discussion</b>	<b>36</b>
4.1	Tissue mimicking phantom scans . . . . .	36
4.1.1	Arrival time based shear modulus estimates . . . . .	36
4.1.2	Direct inversion based shear modulus estimates . . . . .	36
4.2	In-vivo calf muscle scans . . . . .	37
<b>5</b>	<b>Conclusions</b>	<b>39</b>
<b>Bibliography</b>		<b>41</b>
<b>Appendices</b>		
<b>A Risk assessment evaluation</b>		<b>42</b>
<b>B Noise robust ratio estimator derivation</b>		<b>43</b>

## NOMENCLATURE

$\delta_{ij}$	Kroenecker delta function
$\epsilon_{ijk}$	Levi-Cita / permuation symbol
$\partial_i$	partial spatial derivative with respect to $x_i$
$i, j, k, l$	index variables $\in \{1, 2, 3\}$ , repeated indices imply summation
$x_i$	$i^{\text{th}}$ spatial coordinate
$\ddot{\phi}$	second partial derivative with respect to time of $\phi$
$E$	elastic modulus
$b_i$	body force per unit mass at a point along the $x_i$ axis
$\rho$	local mass density
$u_i$	displacement of a point from its non-deformed position using a Lagrangian description along the $x_i$ axis
$\lambda$	Lamé's first parameter
$\mu$	Lamé's second parameter (shear modulus)
$\nu$	Poisson's ratio
$C_{ijkl}$	stiffness tensor component relating $\sigma_{ij}$ and $\varepsilon_{kl}$
$\varepsilon_{kl}$	infinitesimal strain at a point acting on a plane normal to the $x_k$ axis along the $x_l$ axis
$\sigma_{ij}$	stress at a point acting on a plane normal to the $x_i$ axis along the $x_j$ axis

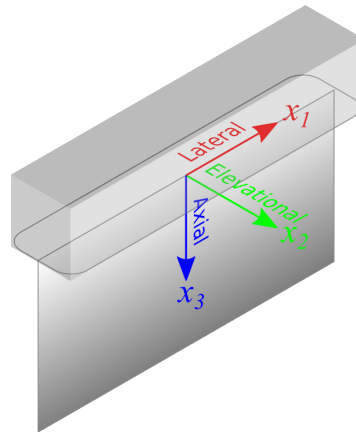


Figure 1: Schematic of ultrasound probe coordinate system with respect to imaging plane (gradiated rectangle) and probe (grey box)

# 1. INTRODUCTION

## 1.1 Problem overview

It has long been known that the mechanical properties of soft tissues, particularly their stiffness, are characteristic of some pathologies. For example cancerous lesions are often much stiffer than the surrounding tissue [1], and diseases such as liver cirrhosis are associated with an increase in stiffness in the affected region, with a strong positive correlation between the severity of the cirrhosis and measured liver tissue stiffness [2]. Quantitative measurements of tissue stiffness can be used therefore to help identify the onset of such pathologies and track their progression.

Techniques for measuring tissue stiffness are therefore of significant diagnostic potential. The most common method is manual palpation, which allows subjective assessment of the stiffness distribution in a region. Either pressure is applied with the hands externally or internal structures such as organs in the abdominal cavity are palpated during surgical interventions [3].

Although it remains an important diagnostic technique, the scale of and depth to which structures can be identified by external palpation are inherently limited and palpation of internal body tissues during surgical operations is obviously an undesirably invasive and risky technique.

These limitations have motivated the development of techniques for non-invasive imaging of tissue elastic properties, often termed elastography. There is an expanding body of research on the development of elastography methods - what will follow now is a brief overview of the various approaches to elastography, followed by a review of the ultrasound based methods which will form the basis of much of the work in this project.

## 1.2 Elastography fundamentals

All elastography techniques share the following common basis:

- mechanical excitation of the tissue
- measurement of tissue displacements induced by the excitation
- estimation of the elastic properties of the tissue given the measured displacements

The various elastography approaches can be categorised by the differences in the implementation of these elements, with usually the method used to calculate the tissue elastic properties being decided by the first two elements.

### 1.2.1 Imaging modality

One distinguishing factor is the choice of imaging modality for observing the tissue displacements. The two main modalities used are *Magnetic Resonance Imaging* (MRI) and

ultrasonography. Optical [4] and mechanical [5] based imaging methods are also possible however neither has yet found widespread adoption nor is relevant to this project and so they will be ignored here.

### Magnetic Resonance Elastography

*Magnetic Resonance Elastography* (MRE) uses phase-contrast MRI techniques to track harmonic tissue motion. MRE offers the advantage of allowing acquisition of displacement measurements for structures deep within the body. A key advantage is that it allows recovery of all three components of the displacement vector field [3, 6]. A major disadvantage of MRE is the long data acquisition time which is inconvenient to the patient, prevents real-time imaging and creates issues in correcting for the effect of independent patient motion. MRI equipment also has high capital and operating costs compared to ultrasound hardware, and is less widely available in clinical environments.

### Ultrasound Elastography

In ultrasound elastography, tissue motion is measured either using displacement tracking schemes on ultrasound *radio frequency* (RF) data or less commonly by using Doppler-effect techniques to directly estimate local tissue axial velocity components.

Ultrasound based techniques typically have much quicker acquisition times than MRE, with real-time imaging often feasible. Generally the estimates of non-axial tissue displacements will be poor or non-existent, with lateral displacement estimates suffering from the reduced resolution of ultrasound imaging in the lateral dimension, and the elevational component only available when three-dimensional scanning techniques are used. This restriction to one or two components of displacement data requires further assumptions in the tissue mechanical model to produce a tractable inversion problem.

The large change in acoustic impedance on moving from soft tissue to bone typically prevents the penetration of ultrasound beyond bone surfaces with similar problems with gas-filled regions such as parts of the digestive tract and the lungs. The overall penetrative power of ultrasound is also reduced compared to MRI - at the frequencies required for reasonable spatial resolution, the attenuation of ultrasound in soft tissue limits scans to a depth of around 15 cm at maximum [6].

Despite these limitations, ultrasound based elastography techniques are popular, with the lower costs, ease of operation and potential for real-time imaging outweighing the benefits of the higher quality data of MRE in many applications.

#### 1.2.2 Tissue excitation method

The other major categorising factor for the various elastography approaches is how the tissue is mechanically excited during the imaging.

## **Static and dynamic loading**

In static, more accurately quasi-static, elastography techniques, a compression is applied to the tissue which is assumed to be sufficiently slowly varying such that inertial terms are negligible and static analysis techniques can be used [7].

In dynamic elastography techniques, forces with significant temporal variation are used. These can be sub-divided into techniques which use harmonic tissue excitation, typically allowing the tissue to come to some steady state, and techniques which use transient forces.

## **Internal and external excitation**

Elastography techniques also differ in whether the forces are applied externally - e.g. by applying pressure with an ultrasound probe or using a vibrating actuator - or internally, with some ultrasound elastography techniques using high intensity ultrasound waves to induce motion (often termed *Acoustic Radiation Force Impulse (ARFI)*) and other techniques exploiting natural respiratory or cardiac motion.

## **1.3 Review of relevant existing techniques**

In this project ultrasound elastography techniques will be considered for measuring tissue stiffness. The intention is develop a hybrid method exploiting some of the advantages of two existing techniques. An overview of these technique follows.

### **1.3.1 Window similarity based displacement estimation**

Aside from a few Doppler-effect based approaches, nearly all ultrasound elastography approaches use a similar technique to compute the underlying displacement field estimates.

Consider a typical case of tracking displacements axially between two 2-D scans, one of which is acting as a reference which the displacements are with respect to. The reference scan is divided into a set of small, generally overlapping, rectangular windows. For each window the displacement estimate is initialised, for example to the value of the nearest previous reliable estimate, or to zero if at the top of the scan. From that starting point a search is conducted for the maximum of a similarity measure computed between the reference window, and a corresponding window from the second scan, centred at the reference window position plus an offset equal to the current displacement estimate. Sub-sample precision can be achieved by interpolating either the similarity measure to find the maximum or the scan data prior to windowing. There are a variety of possible similarity measures that can be used to determine the fit between windows - the most common are cross-correlation, sum of absolute or squared differences and correlation phase matching [7].

### 1.3.2 Quasi-static ultrasound elastography

*Quasi-static Ultrasound Elastography* (QUE) is a well-established technique that can produce real-time high-quality images of relative tissue ‘stiffness’ and importantly can be implemented using just standard ultrasound hardware [7].

In QUE the tissue is deformed by a slightly varying pressure applied by the face of the probe. For moderate scan depths (up to 5 cm) physiological tremor can provide sufficient pressure variation [7]. The above window matching technique is used to generate displacement estimates, either between each recorded scan frame and a fixed reference frame, or between the current frame and a reference at a fixed offset. The strain field, which is the displacement gradient, is then estimated by numerical differentiation with a filtering operation.

In some cases except normalisation by a constant the strain images are displayed directly as these can convey sufficient information about local tissue stiffness (often a region undergoing high strain will have a low stiffness and vice versa) [7]. To generate truer approximations of tissue stiffness, a model of the stress distribution through the scanned region can be calibrated to the data. The ratio of these modelled stress values to the estimated strains can be displayed as relative stiffness estimates.

Importantly without knowledge of stress or stiffness boundary conditions only relative measures of elasticity can be deduced. While the resulting images still allow identification of regions of high stiffness, the lack of a quantitative component to the data prevents classification of observed structures by comparing the measured stiffness estimates with known values.

### 1.3.3 Dynamic ultrasound elastography

The limitation of QUE to giving only relative measurements is a fundamental issue with the static analysis techniques it uses. Dynamic ultrasound elastography techniques which are instead based on imaging shear wave propagation in soft tissue overcome this problem.

By assuming some mechanical model, the equations of motion governing wave propagation can be derived and used to relate the measured internal displacement fields in a tissue region to its mechanical properties. As a partial differential equation formulation of the governing equations of motion is inherently local in character, it can be used as a basis for local estimation of the tissue mechanical properties, and in particular stiffness, given the measured tissue displacements.

A variety of dynamic ultrasound approaches have been developed. The pulsed transient shear wave imaging [8] method developed by Fink et. al. and the later supersonic shear imaging [9] technique introduced by the same group have been particularly successful [3]. By exploiting special high power and frame-rate ultrasound hardware, these techniques can provide high resolution, quantitative stiffness images of a region.

## Pulsed transient elastography

*Pulsed Transient Elastography* (PTE) is a dynamic elastography approach based around the measurement of the displacements induced by pulsed low frequency shear waves [10, 8]. The shear waves are generated by a vibrating device consisting of linear actuators on either side of the imaging probe and parallel to its lateral axis. The actuators are driven with a single period of a 50 Hz sinusoid, with around a 1 mm amplitude, acting axially. The set-up geometry is such that the shear wavefronts constructively interfere to create a quasi-linear longitudinally-polarised shear wavefront in the imaging plane.

Although shear waves travel at much slower velocities in soft tissue than compression waves ( $\sim 5 \text{ ms}^{-1}$  versus  $\sim 1500 \text{ ms}^{-1}$ ), even at this reduced speed a shear wave will cross a typical 5 cm extent of a probe's imaging region in around 0.01 s. Conventional ultrasound scanners acquire images by sequentially sending pulses out from a linear array of transducer elements and then waiting for the return of echoes from those pulses. For a 128 element probe scanning up to depths of 5 cm this gives an acquisition time of just under 0.01 s per scan frame. Evidently this is too slow to capture sufficient information about shear wave progression across the imaging plane.

To overcome this problem, Fink et. al. developed a special high frame rate ultrasound system which avoids transmission stage focussing. This system simultaneously transmits from all elements in a mass pulse and writes the received echo signals to memory buffers for each element. Once sufficient time has been left for echoes to be received from the desired scan depth, another mass transmit and receive can be initiated. The signal data is then focussed post-acquisition using a delay-and-sum parallel beam forming method. For a 7.5 cm scan depth this allows the scanner to operate at around 10 000 frames  $\text{s}^{-1}$ .

The ultrasound RF frames produced using this scanner and actuator combination are used to estimate displacements with the window matching method described earlier. This gives a temporally and spatially dense set of measurements of the displacement response as the shear wave travels along the imaging plane. In order to estimate the local tissue stiffness distribution the PTE paper [8] details a method for direct inversion of the governing wave equation of a simplified model for the tissue. This will be discussed in section 2.2.

## Supersonic shear imaging

*Supersonic Shear Imaging* (SSI) [9] is a more recently developed transient elastography technique, which exploits the same high-speed ultrasound imaging system as PTE but uses a different method for inducing the shear waves to overcome some of the limitations of the external vibrator based method. In particular the added weight and bulk of the actuators makes probe usage more awkward, and the external excitation has limited penetration in some highly attenuating tissues such as breast [9].

In SSI, ARFI techniques are used to remotely induce a low-frequency dipolar shear-

wave source within the imaged tissue region. By altering the focus to move the source at supersonic speeds (i.e. greater than the shear wave velocity in the tissue), the shear waves can be made to constructively interfere along a Mach cone, creating two opposing quasi-planar shear wavefronts. The fast imaging system can then be used to capture the wavefront progression through the tissue.

There are two main approaches used to recover an estimate of the local tissue mechanical properties given the measured displacement fields for SSI. In the original SSI paper [9], the same inversion technique as proposed in the earlier PTE work is again set out as the method used to produce stiffness images. Later works [11, 12] indicate a switch to a method based on tracking wavefronts through the tissue to estimate their arrival times at each spatial location. The inversion and arrival time techniques will be discussed in sections 2.2 and 2.3 respectively.

## 1.4 Project motivation and aims

In the preceding section it was observed that:

- QUE is a good technique for producing images of relative stiffness in a region of interest and requires only conventional ultrasound hardware, but without further information cannot give quantitative stiffness information
- dynamic ultrasound elastography techniques such as PTE and SSI, can produce absolute stiffness images but require specialist hardware

An imaging technique using only standard ultrasound hardware that allows full quantitative imaging would be preferable. The aspects of discussed dynamic elastography techniques requiring non-standard hardware were:

- generation of a shear wavefront using either mechanical actuators attached to the probe or a high-power transmit mode on the probe to remotely induce shear waves using ARFI techniques
- use of a high-speed scanner to allow imaging of a propagating shear wavefront at a sufficient rate to adequately characterise its motion

Although the methods for inducing shear waves used in the existing dynamic techniques have the advantage of producing consistent and near planar shear wavefronts, it is proposed that a simpler way of generating shear waves in tissue may be to apply an impulse at a point on the surface - i.e. to tap it. Although the displacement wave behaviour generated by such a disturbance may be more complex, it should still be governed by the local mechanical tissue properties. The first novel contribution in this project will therefore be to attempt recovery of tissue stiffness values from measurements of wave displacements created by manually tapping the tissue surface.

The second contribution proposed in this project is to attempt to track the progress of a shear wave with a conventional ultrasound scanner by scanning across only a subset of the total array of transducer elements and therefore achieving a much quicker ‘frame-rate’. If this sparser set of scan data can be used to estimate local tissue stiffness at only a few locations these quantitative point measurements could then be used to fix the unknown scale on a relative stiffness image of the same region produced using the standard QUE technique.

The aims of the project are therefore:

- to explore techniques using only conventional ultrasound hardware of estimating absolute shear modulus within a region of interest by analysing the dynamic displacement response to a surface tap.
- to integrate the developed technique with the existing QUE method and use the sparse set of absolute point measurements to calibrate the relative field to produce a full absolute stiffness image.

## 2. THEORY

To clarify the experimental work done in developing the proposed elastography method, some theoretical background of the techniques being used will now be discussed.

### 2.1 Tissue mechanical model

An essential element of elastography techniques is a mechanical model for the soft tissue being observed. This allows what is measured - tissue displacements, to be related to what is required - local tissue mechanical properties, with the former used to infer the latter. In order to achieve this, the model used must be simple enough to be fully constrained by the obtainable empirical data. This necessitates making simplifying assumptions about tissue mechanical behaviour.

#### 2.1.1 Assumptions

##### Zero body forces

The magnitude of body forces such as tissue self-weight will be assumed to be negligible and so ignored. This is a standard assumption in elastography techniques and is unlikely to significantly affect model accuracy. The main restriction it places on the validity of the model is that only the displacements measured after the initial forcing tap has ended should be used when estimating the tissue mechanical properties.

##### Linear elasticity

A linear tissue deformation response will be assumed. This is a reasonable simplification for small deformations, though as the displacement magnitude increases the model will become increasingly inaccurate as soft tissue exhibits significant non-linearities for large strains [3]. Under this assumption the relation between the stress and strain tensors at a point is  $\sigma_{ij} = C_{ijkl}\varepsilon_{kl}$  with  $C_{ijkl}$  the fourth-order stiffness tensor. An infinitesimal definition of the strain tensor is used

$$\varepsilon_{kl} = \frac{1}{2} (\partial_k u_l + \partial_l u_k).$$

Although viscous effects are significant in soft tissues, in this project an elastic simplification will be used as a first order approximation in common with the model used in PTE [8] among others. This is partly justified by the use of a low-frequency excitation method which should reduce wave attenuation. In this case the stiffness tensor coefficients are real.

##### Local homogeneity

The tissue mechanical properties will be modelled as being locally homogeneous such that they can be considered (piecewise) constant at each displacement estimate position and

their derivatives neglected. This is an important assumption as it provides the potential of direct algebraic inversion of the governing equation [3] to form point estimates of the mechanical properties rather than solving for continuously varying parameters.

The validity of this assumption depends on the window size used to estimate the displacements - if the variation in tissue mechanical properties across the windows is non-negligible the assumption of local homogeneity will be invalid, and so on this basis smaller window sizes are better. Small windows will however decrease the accuracy of the displacement estimates as there is an increased probability of false matches. For windows located on discontinuities in the tissue mechanical properties, the assumption will be poor for any reasonable window size. It will be necessary to consider this when analysing parameter estimates made in such locations.

## Isotropy

The tissue will be modelled as isotropic. In this case the stiffness tensor can be characterised by two values - Lam  s first parameter  $\lambda$  and Lam  s second parameter  $\mu$  (or equivalently shear modulus) -  $C_{ijkl} = \lambda\delta_{ij}\delta_{kl} + \mu(\delta_{ik}\delta_{jl} + \delta_{il}\delta_{jk})$ . Isotropy is a reasonable approximation for some soft tissues such as breast and liver but is a poor model for fibrous tissues like muscle [13].

## Incompressibility

Soft tissues have a high water content and typically have a Poisson's ratio in the range  $0.4900 \leq \nu \leq 0.4999$  [14]. This implies soft tissues are near incompressible and as  $E = 2\mu(1 + \nu)$  and  $\lambda = \frac{2\mu\nu}{1-\nu}$  that  $E \approx 3\mu$  and  $\lambda \gg \mu$ . Under this (and the previous assumptions) tissue can be characterised by a single elastic parameter and estimation of the shear modulus  $\mu$  will directly lead to estimates of tissue stiffness  $E$ . Importantly the displacement field in incompressible materials is divergence free i.e.  $\partial_i u_i = 0$ .

## Constant density

Due to high water content soft tissue density variation is small and an approximation of  $\rho(x_1, x_2, x_3) \approx \rho_{\text{water}} = 1000 \text{ kg m}^{-3}$  will be used.

### 2.1.2 Governing equation

Using these assumptions, the equation governing the small-displacement motion of soft tissue will now be derived. The starting point for this will be the differential form of the principle of conservation of linear momentum

$$\partial_j \sigma_{ij} + \rho b_i = \rho \ddot{u}_i.$$

ASSUMPTION 1: Zero body forces	$b_i = 0$
--------------------------------	-----------

$$\partial_j \sigma_{ij} = \rho \ddot{u}_i$$

ASSUMPTION 2: Linear elasticity

$$\sigma_{ij} = C_{ijkl}\varepsilon_{kl} \quad C_{ijkl} \in \mathbb{R}$$

$$C_{ijkl}\partial_j\varepsilon_{kl} + \varepsilon_{kl}\partial_jC_{ijkl} = \rho\ddot{u}_i$$

ASSUMPTION 3: Local homogeneity

$$\partial_jC_{ijkl} = 0$$

$$C_{ijkl}\partial_j\varepsilon_{kl} = \rho\ddot{u}_i$$

DEFINITION: Strain tensor

$$\varepsilon_{kl} = \frac{1}{2}(\partial_k u_l + \partial_l u_k)$$

$$\frac{1}{2}C_{ijkl}\partial_j(\partial_k u_l + \partial_l u_k) = \rho\ddot{u}_i$$

ASSUMPTION 4: Isotropy

$$C_{ijkl} = \lambda\delta_{ij}\delta_{kl} + \mu(\delta_{ik}\delta_{jl} + \delta_{il}\delta_{jk})$$

$$\lambda\partial_i\partial_j u_j + \mu(\partial_j\partial_j u_i + \partial_i\partial_j u_j) = \rho\ddot{u}_i$$

ASSUMPTION 5: Incompressibility

$$\partial_j u_j = 0$$

$$\mu\partial_j\partial_j u_i = \rho\ddot{u}_i$$

## 2.2 Inversion based methods

Using the result just derived and considering only the axial direction with coordinate system as in figure 1

$$\mu\nabla^2 u_3 = \rho\ddot{u}_3$$

Rearranging this gives the following equation for  $\mu$

$$\mu = \rho \frac{\ddot{u}_3}{\nabla^2 u_3} \tag{2.1}$$

This is the basis of the direct inversion technique proposed in the PTE [8] and SSI [9] papers. These papers further assume that

$$\frac{\partial^2 u_3}{\partial x_2^2} \ll \frac{\partial^2 u_3}{\partial x_1^2} + \frac{\partial^2 u_3}{\partial x_3^2} \Rightarrow \nabla^2 u_3 \approx \frac{\partial^2 u_3}{\partial x_1^2} + \frac{\partial^2 u_3}{\partial x_3^2}$$

with limited justification given in terms of symmetry conditions. Perhaps more importantly, as ultrasound imaging is typically limited to scanning two dimensionally, estimates of the spatial derivatives in the elevational direction cannot be recovered. Under this assumption, equation (2.1) gives a relationship between the parameter which it is wished to estimate  $\mu$  and spatial and temporal (second) derivatives of the measured  $u_3$  which can be estimated using numerical techniques. Presumably to provide some noise robustness [8] and [9] recommend averaging the estimate of  $\mu$  from all  $N$  collected displacement field frames, such that if  $f$  is an index for the frame recorded at time  $t_f$  then

$$\mu(x_1, x_3) \approx \rho_{\text{water}} \frac{1}{N} \sum_{f=1}^N \left( \frac{\frac{\partial^2 u_3}{\partial t^2} \Big|_{x_1, x_3}}{\frac{\partial^2 u_3}{\partial x_1^2} \Big|_{t=t_f, x_3} + \frac{\partial^2 u_3}{\partial x_3^2} \Big|_{t=t_f, x_1}} \right)$$

### 2.3 Arrival time based methods

The governing equation of motion derived earlier for each of the three displacement components can be rearranged in to the standard form of a homogeneous scalar wave equation. Considering only the axial component

$$c_s^2 \nabla^2 u_3 - \ddot{u}_3 = 0 \text{ with } c_s = \sqrt{\frac{\mu}{\rho}}.$$

As the name suggests, solutions to the wave equation are of the form of travelling waves, under the model assumed the wave velocity being  $c_s$ . It can therefore be seen that the local velocity of shear waves observed travelling through the tissue are directly related to the local shear modulus (given the assumption  $\rho$  is fixed and known).

A basic algorithm for estimating the absolute shear modulus in a scanned region (and so using  $E \approx 3\mu$  stiffness) is to estimate the times at which a wavefront arrives at different known locations in the scanned region.

Assume the wavefront is travelling along the lateral direction through the image plane and that it arrives at the line  $x_1 = X$  at time  $t = T$  and at the line  $x_1 = X + \Delta X$  at time  $t = T + \Delta T$ . Then a zeroth order approximation of the shear wave velocity between those two lines is

$$c_s \approx \frac{(X + \Delta X) - X}{(T + \Delta T) - T} = \frac{\Delta X}{\Delta T}.$$

Using the expression for  $c_s$  above

$$\mu \approx \rho \left( \frac{\Delta X}{\Delta T} \right)^2.$$

Therefore if the differences in arrival time of a wave travelling along the lateral axis of the ultrasound probe at known locations along the probe can be calculated, the shear modulus between those points can be estimated. In this zeroth order approximation, it has been assumed the shear velocity is constant between the measurement points. For non-homogeneous tissues, the accuracy of this approximation will depend on the separation  $\Delta X$  with greater validity for small separations. However the noise component in  $\Delta T$  increases as the separation becomes smaller.

In [11] a more rigorous treatment of the problem of recovering local shear moduli values given the arrival times of wavefronts generated by transient excitation of a tissue region is presented. The important result derived is that the local arrival times  $\hat{T}(x_1, x_2)$  of the shear wavefronts in the imaging plane  $(x_1, x_3)$  satisfy a form of standard partial differential

equation termed an Eikonal equation (over the domain  $\mathcal{S} := \{x_1, x_2 : \exists u_1(x_1, x_2, t) \neq 0\}$ )

$$|\nabla \hat{T}| = \sqrt{\frac{\rho}{\mu}} = \frac{1}{c_s}.$$

Intuitively it is evident that this corresponds to the limit of  $\Delta X \rightarrow 0$  in the above approximation and generalising to the two dimensional case where the wave propagation direction may be arbitrary.

To estimate the arrival times from the measured displacement data, [11] suggests a correlation maximisation technique. In particular the cross-correlations of a reference wave displacement-time profile measured at a location near the wave source with the displacement-time profile at each other spatial location are computed, and the arrival time chosen as the time offset from the reference wave which maximises the cross-correlation at each location.

The use of cross-correlation is motivated by its non-reliance on a particular wave profile form, its invariance to amplitude changes and its provision of a reasonable solution when matching wave profiles which have undergone some dispersion, the latter two both important given the attenuation and scattering waves undergo when propagating in real tissues.

## 2.4 Finite difference simulation

In order to test and develop the shear modulus estimation techniques used in this project, it was clear that it would be useful to have synthetic displacement data corresponding to excitations of known shear modulus distributions available. This could then be used as ‘ground truth’ to test the performance of the developed techniques. To this end various acoustic wave equation modelling options were considered.

The chosen solution was the MATLAB script detailed in [15]. Although originally written for the purposes of seismology research, the general nature of the method of specifying a model in the script made it simple to use on much smaller scale acoustic models. Some changes were made to the code to increase computational efficiency by reducing the update code for the original full anisotropic model to a simplified version appropriate for the isotropic mechanical model being used here.

An additional mode for shear-wave only simulation (by applying the incompressibility assumption) was added to the existing simulation with both compressional and shear wave components. This was necessary because of the large difference in the compressional and shear wave speeds in the soft-tissue materials being simulated, with inclusion of compressional terms therefore requiring a much smaller time-step than is necessary for a shear-wave only simulation because of the higher wave speeds involved.

### 3. DEVELOPMENT OF METHOD

In the following section, the work done on developing the new technique will be presented through three main strands:

1. implementing the displacement response measurement using a custom ultrasound scan sequence
2. investigating the practicalities of using a manual tap as a excitation method
3. developing and testing the different approaches to estimating shear modulus from the measured displacements

#### 3.1 Displacement measurement

##### 3.1.1 Scan sequence choice

The method proposed in this project for obtaining displacement field estimates with sufficient temporal resolution is to scan across only a subset of the full array of probe element positions. Fundamental to the developed method therefore is the choice of which sequence of elements to scan over.

###### Direct inversion data scan sequence

For the inversion method (section 2.2) it is preferable to use small lateral separations between the scan element positions to minimise the approximation error in the finite difference operations applied to the displacement data. Thus scanning over adjacent element positions is appropriate in this case. Data at a minimum of three lateral positions is required to compute the second order finite difference of the displacement field in the lateral direction, with more points being preferable to allow smoothing. Competing with this is the need to minimise the scan sequence length so that the time between successive measurements at each location, and so the approximation error in the temporal second derivative, is small.

In consideration of the balance of these competing factors and a preference for using sequences of lengths that are integer powers of two for implementation reasons, it was decided to use a scan sequence consisting of eight adjacent probe element locations at the centre of the array.

###### Arrival time data scan sequence

For the arrival time method (section 2.3) it is advantageous to have greater separations between the scan element positions so the differences in the arrival time of a wave travelling across the imaging plane are measurable and have a reasonable *Signal-to-Noise-Ratio* (SNR). Increase in the scan element position separations will however lead to an increase in the approximation error due to the constant velocity between scan points assumption,

Parameter	Value	Justification
Ultrasound wave speed	1540 ms <sup>-1</sup>	Soft tissue average
Shear Wave speed	2.89 ms <sup>-1</sup>	Theoretical shear wave speed for phantom background elastic modulus 25 kPa
Pulse frequency	30 Hz	Tap expected to produce low frequency wave pulse / comparable to PTE value
Attenuation coefficient	0.5 db cm <sup>-1</sup> MHz <sup>-1</sup>	Value for phantom background material
Ultrasound frequency	3 MHz	Typical clinical ultrasound value
SNR at probe face	50	Optimistic estimate for best-case analysis

Table 3.1: Initial simulation parameters and justification

and there is again a trade-off in the choice of scan sequence length between temporal resolution and spatial extent of the data.

A MATLAB simulation was developed to help better understand how the choice of scan sequence affects the usefulness of the displacement estimates produced. This simulated the displacement data measured when scanning a specified space-time displacement field, by spatially and temporally sampling the field according to when information about a particular point would become available from the echo of an ideal ultrasound pulse travelling to and from the probe. The displacement measurements were modelled as being subject to additive Gaussian noise, with exponential scaling to account for the decreased SNR at greater depths due to signal attenuation.

An empirical model was used to produce the displacement field as this work was done prior to the development of the FTD wave simulator. The model consisted of a planar wavefront of fixed displacement profile travelling along the lateral axis. Displacements were in the axial direction, with a single sinusoid period pulse shape. Although simplistic the intention here was not to accurately model a propagating shear wavefront, but to give a vaguely plausible and easily calculable displacement field.

The parameters of the model, shown in 3.1 were chosen to match the properties of the tissue mimicking phantom used for later experimental work. After testing various scan sequences, it was decided a four-element sequence with the element positions equally spaced across the probe array minus a small ‘buffer’ at either end to allow for the aperture width would give a good balance between the competing factors. The model runs for this sequence (example in figure 3.1) suggested there would be around 10 measurement time steps (i.e. time gap between successive displacement measurements at same position) between the arrival of the wavefront at successive scan locations, allowing the wave arrival times to be computed to within a 10% error. Scanning at four different locations allows some coarse lateral localisation of any shear modulus estimates produced.

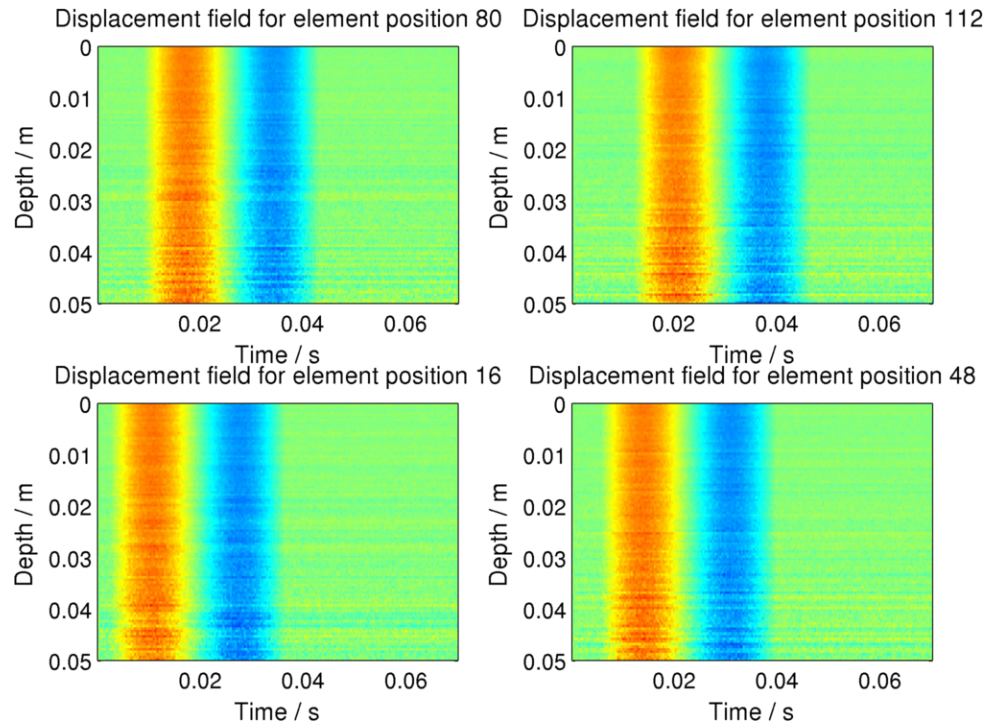


Figure 3.1: Simulated displacement fields measured at different elements

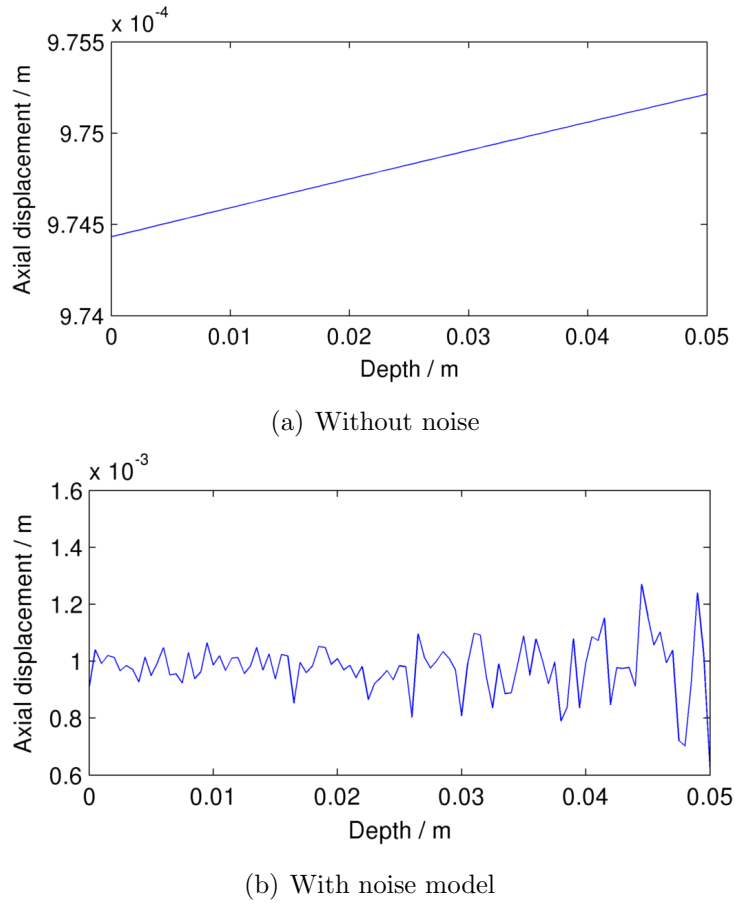


Figure 3.2: Comparison of simulated axial displacement plots for scan line recorded at element position 0.01s at element position 16. Note difference in vertical scales of plots.

The model runs also suggested that it would not be particularly important to consider the order in which the probe locations are scanned over in reference to the wave travel direction, as the effective lateral scan speed is much more than the expected wave velocities and any discrepancy will be negligible compared to the error introduced by the discretisation of the arrival time estimates. Similarly the effect of the progression of the wave in between axial measurements appeared to be negligible, with the small trend introduced in to the displacement profiles along axial scan lines insignificant compared to the modelled measurement noise as shown in figure 3.1.1.

### 3.1.2 Implementation details

#### Hardware

The diagnostic ultrasound imaging system used as the basis for all the experimental work in this project was the *Ultrasonic Sonix RP*, used in conjunction with a *Ultrasonix L14-5/38* probe, which is a linear-array type with 128 ultrasound transducer elements.

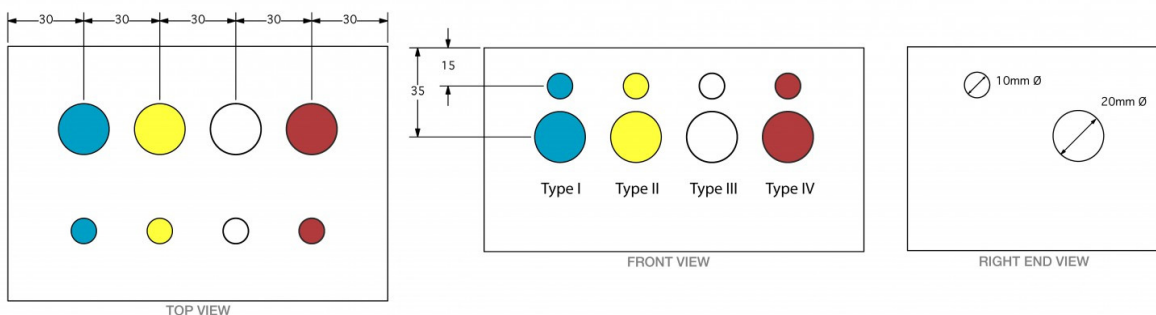


Figure 3.3: Schematic of phantom showing positions and sizes of spherical inclusions.  
Image credit: Computerized Imaging Reference Systems Inc.

The target of most of the scans made in this project was a *CIRS Model 049 Elasticity QA Phantom* of known elastic modulus distribution. The phantom consists of a uniform block of Zerdine tissue mimicking material of elastic modulus  $E_b = 25 \pm 4 \text{ kPa}$  containing a set of eight spherical inclusions of four elastic moduli ( $E_I = 8 \pm 3 \text{ kPa}$ ,  $E_{II} = 14 \pm 4 \text{ kPa}$ ,  $E_{III} = 45 \pm 5 \text{ kPa}$ ,  $E_{IV} = 80 \pm 8 \text{ kPa}$ ) and two sizes. The phantom is rigidly constrained on all sides except the top surface. The ultrasound wave speed in the background material and inclusions is nearly constant at  $1545 \pm 10 \text{ ms}^{-1}$ , closely matching the standard figure for soft tissues.

#### Software

*Stradwin* a research oriented ultrasound imaging package was used to acquire the ultrasound data and process it to produce displacement estimates. The software includes an inbuilt strain imaging mode designed for QUE use, however by disabling the derivative estimation and normalisation steps it is possible to output raw displacement measurements.

Parameter	Choice
Displacement tracking algorithm	Weighted Phase Separation + Amplitude Modulation Correction [16]
Windowing direction	Axial only (1D)
Window size	1.03 mm
Window overlap	50%
Tracking initialisation	Top, zero
Gradient filter length	0 (i.e. displacement measurement)
Normalisation	None

Table 3.2: Stradwin strain estimation dialog settings

### Custom scan sequences

The required custom scan sequences were implemented by adding creating a new Stradwin scan mode using the *Ultrasonix Texo* development toolkit. Following from the discussion in the previous section the centre element positions of main scan sequences used were:

- scan sequence for arrival time data [ 16 48 8 112 ]
- scan sequence for direction inversion data [ 60 61 62 63 64 65 66 67 ]

where the indices indicate the array position at (the centre of) the specified element with the elements being numbered from 0 to 127. Data is captured in ‘frames’ of 128 scan-lines, consisting of the 128 sampled received RF signals for the specified scan sequence. The scan-sequences were implemented so that the probe sequentially scanned over the specified positions in a loop, so that each data frame was recorded in a sequential manner. For example for the first scan sequence above, the element positions of the recorded data frame would be of the form 16, 48, 80, 112, 16, 48, 80, 112, 16...

A small adjustment was made to the Stradwin displacement tracking algorithm to force it to use the first captured frame of ultrasound RF data for each element as the corresponding reference signal for the displacement tracking algorithm, with the assumption that this was of the scanned region in its undeformed state.

## 3.2 Shear wave generation

A major unknown in this project was whether the use of a manual tap as the tissue excitation method would provide useful displacement data. In this section the work done in exploring the validity of this tissue excitation method and some of the complexities encountered is discussed.

### 3.2.1 Initial phantom tests

To gain a better understanding of if and how tapping the surface of a region of soft tissue produces propagating shear wavefronts, scans of the displacement response of a uniform

region of the phantom to surface taps at two different positions relative to the probe (see figure 3.4) were conducted.

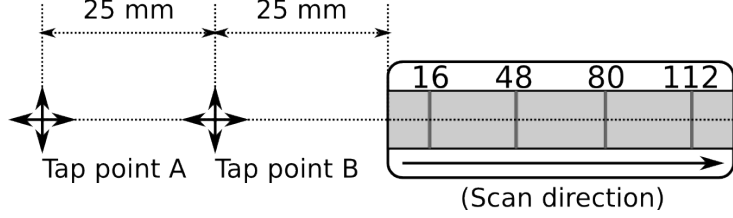


Figure 3.4: Schematic showing location of tap points relative to probe (dimensions indicative rather than exact)

Displacement measurements were made using the four element [16 48 80 112] scan sequence as the intention of this initial batch of tests was to visually analyse the results, with this scan sequence giving more perceptible differences in the displacements measured at the different element positions.

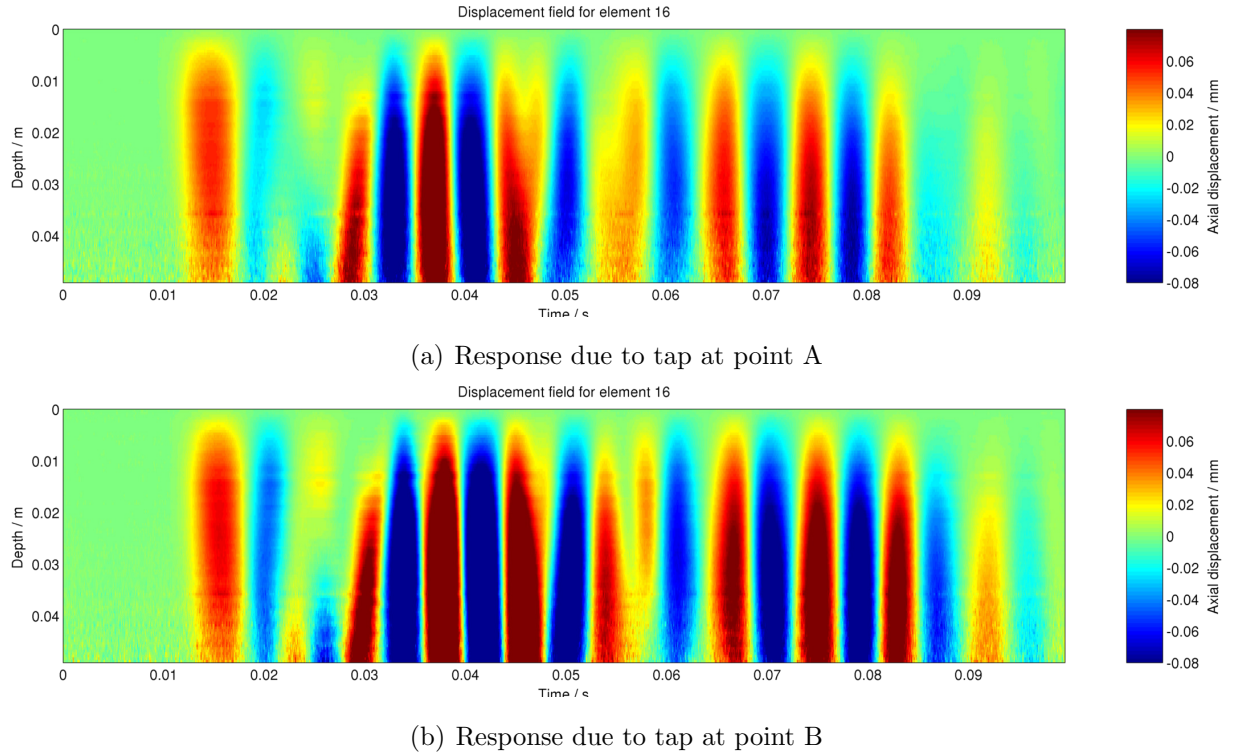


Figure 3.5: Examples of measured axial displacements at element position 16

Figure 3.5(a) shows an example of one of the measured axial displacement fields for a tap at A, measured at element position 16. The origin of the time-scale on the plot is arbitrary, with the initial section prior to the wave arrival removed.

It can be seen that there is a strong, approximately sinusoidal wavefront that passes beneath the probe between around 0.01 and 0.05 s, corresponding roughly to a pulse of

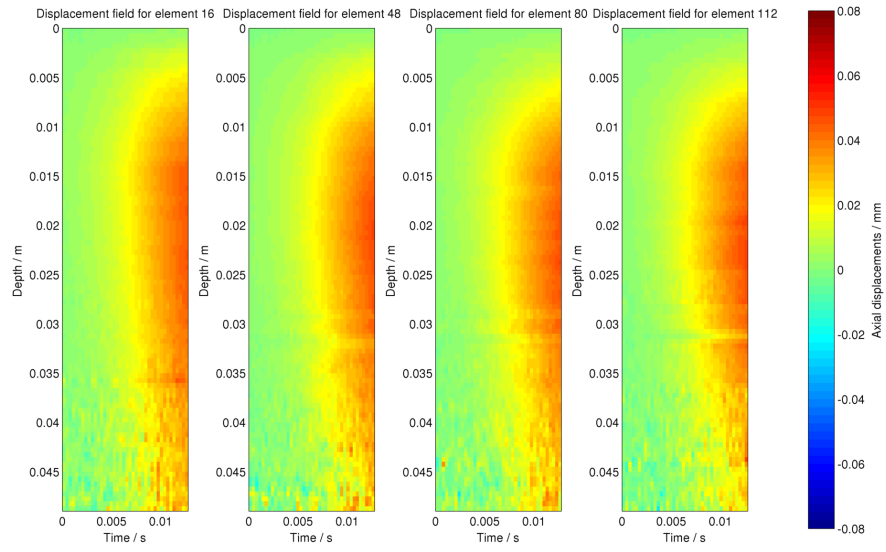
dominant frequency 25 Hz. This compares well with the 50 Hz single-period sinusoid pulse used as the excitation in the PTE method.

As the wave appears to be travelling in a non-axial direction and so perpendicular to the axial deformation, the wave seems to be a shear rather than compressional wave as expected. The wavefront shows little axial variation away from the probe face, with the region closest to the probe showing a decay in the observed deformations in the negative axial direction. This is as would be expected from the confining effect of the probe being held against the phantom surface. Immediately after the initial pass of the wavefront, there is a second lower amplitude wavefront, this believed to correspond to a second period of the initial forward travelling wave pulse. After this, the situation becomes more complex with there being several other passes of wavefronts across the scan line - potentially the result of reflections of the initial wavefront off the rigid boundaries of the phantom.

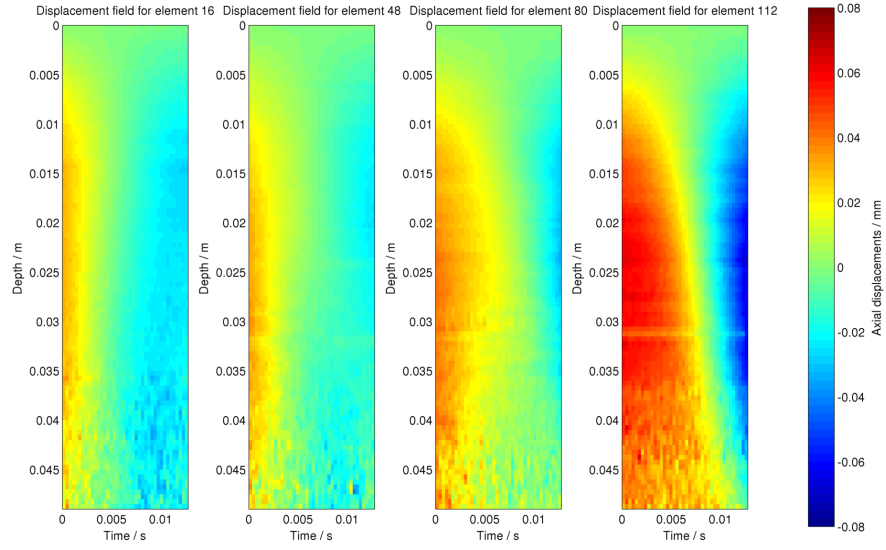
Figure 3.5(b) shows the corresponding axial displacement field measured for a tap at location B. It can be seen that the tissue response for the two taps at different distances from the probe are very similar in form, other than a small increase in the amplitude of the deformation for tap point B compared to A. This suggests over the wave travel distances being considered, dispersive and attenuation effects are minimal, partially validating the use of an elastic rather than viscoelastic model, though in general viscosity effects are observed to be greater in-vivo [8].

Figure 3.2.1 shows small intervals of the displacement response measured at the four element positions for a tap at location A. The interval length corresponds to 40 scan-lines of data measured at each element, this corresponding to the time the initial simulation indicated a shear wave travelling in the lateral direction would take to cross the full extent of the probe's imaging plane. Other than a small shift of 80 ms between each time scale due to the sequential nature of the scanning method, each sets of plots shows the displacement response measured across the same time interval.

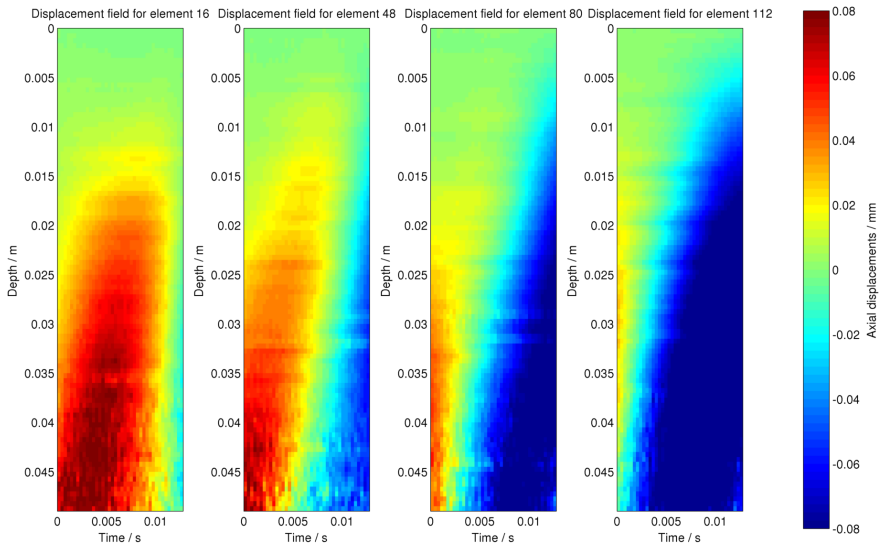
In figure 3.6(a) the initial arrival of the wave at each of the element positions is shown. Counter to what was expected the leading edge of the wave appears to arrive simultaneously at all of the elements. It is not entirely clear what the reason for this is. A possible explanation is that a surface wave component is causing bulk probe motion giving erroneous displacement measurements. More investigation in to this effect is presented in section 3.2.2.



(a) Initial arrival of wavefront



(b) First pass of zero-point of the wave



(c) Subsequent pass of zero-point of the wave

Figure 3.6: Comparison of displacement fields measured at the four element positions across different time intervals for tap location A

Figure 3.6(b) shows the interval in which the zero-point of the wave passes each of the element positions. There appears to be some visible progression in the arrival time of this point on the wave at the different element positions, with as would be expected the zero-point passing the element positions closer to the tap point at earlier times. There are still significant discrepancies from the expected behaviour however with the wavefront not appearing to progress between the element positions with a constant velocity and the arrival time intervals being shorter by around a factor of 3-4 than expected from the initial simulation.

Figure 3.6(c) provides an indication of a possible source for these discrepancies, showing the interval in which a subsequent zero-point of the measured wave pattern passes the different element positions. Here the wavefront appears to be travelling in the *opposite* direction to the scan direction. This suggests this is a reflection that has arrived back at the probe. Such reflections and their interference with the outward travelling wave are outside of the single direction, fixed wavefront model being used for the wave tracking approach.

Some limited testing on the effect of varying the intensity of the tap was also carried out. It was found for low to moderate tap intensity there was little change in the wave pattern observed, other than a decrease in the SNR of the measurements for lower amplitude taps. For very severe taps, the displacement tracking algorithm began to fail at some points in recorded RF data, resulting in ‘drop-outs’ in the estimated displacement data.

### 3.2.2 Effect of probe motion



(a) Probe clamped in position over phantom      (b) Gel layer decoupling probe surface from phantom

Figure 3.7: Probe motion reduction strategies

It was suggested previously that motion of the probe could be behind some of the discrepancies from the expected behaviour observed in the phantom tests. In particular probe motion due to a surface component of the waves travelling from the tap point was

posed as being a possible explanation for the apparent simultaneous arrival of the initial wavefront at all the element scan positions.

For the phantom tests the probe was lightly clamped in place above the phantom as shown in figure 3.7(a). Although more securely fixing the probe might seem an obvious method for eliminating probe motion given that the aim was to investigate a technique that might have future clinical use where rigid probe clamping is unlikely to be viable, it was judged that an alternative to attempting to completely fasten down the probe would be preferable.

In order to maximise the transmission and reception of ultrasound wave pulses between a probe and the scanned material, it is usual to add a thin layer of water-based gel to the surface of the probe to provide improved acoustic impedance matching. It was proposed clamping the probe a few millimetres above the phantom surface with a thicker layer of gel in between would allow the probe to remain acoustically coupled with the phantom material while minimising transmission of mechanical forces. A series of phantom scans were conducted with such a set-up, as illustrated in 3.7(b) and compared to an equivalent set of scans without the gel-layer present.

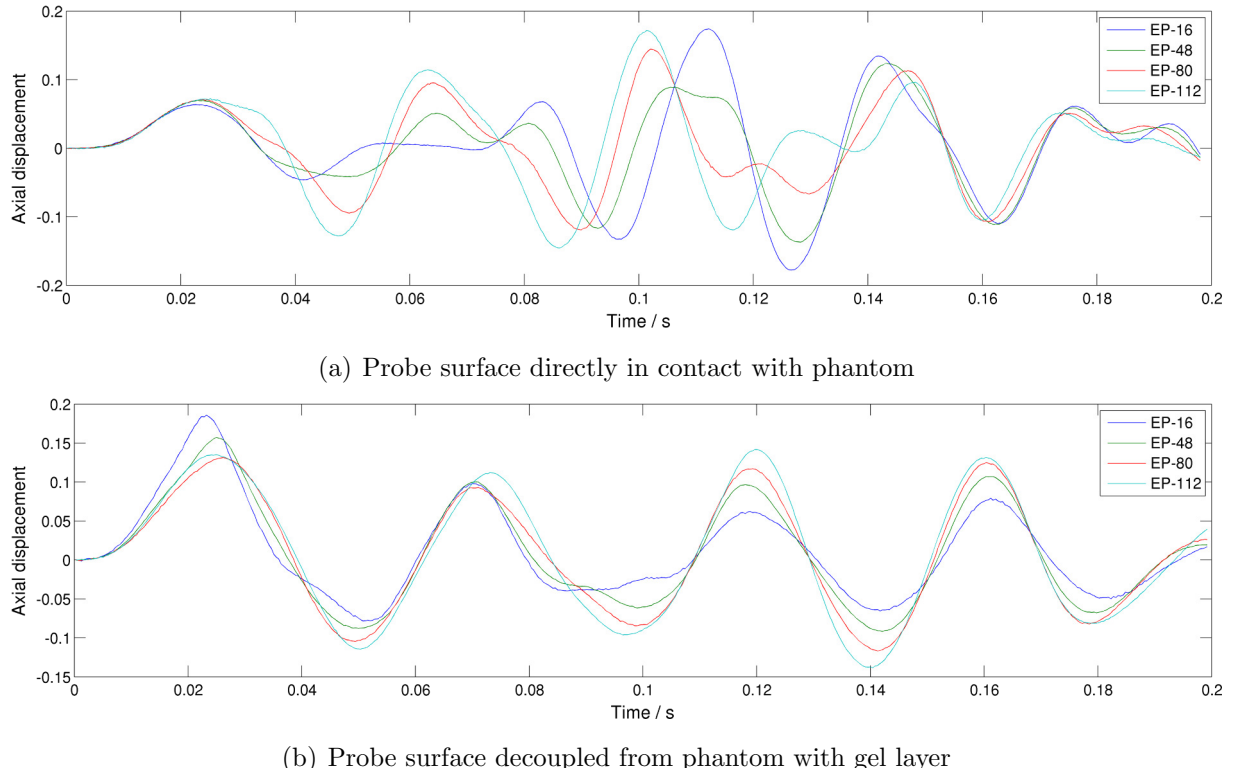


Figure 3.8: Comparisons of displacement responses measured at 2.5 cm depth in uniform region of phantom

Figure 3.8(a) shows the axial displacements measured at a depth of 2.5 cm at four element positions in a uniform section of the phantom with the probe surface in contact with the phantom as was the case in the initial phantom tests.

The discrepancies noted in those initial results are clearly exhibited here as well. The leading edge of the initial wavefront pass appears to arrive at all the probe elements simultaneously and there are significant differences between the forms of the response measured at the different element positions. Even when there does appear to be similarity there is rarely the consistent progression that was expected. Note that although there does appear to be a clear progression between 0.08 and 0.10 s, this is indicative of a wave travelling in the opposite direction to that expected of the original outward wave and it can be seen that there is poor correspondence in the displacement profiles immediately outside this interval, making it unclear whether this result is actually the result of a single travelling wavefront, or a spurious result of interference and/or probe motion.

Figure 3.8(b) shows a corresponding plot when the probe has been mechanically decoupled from the phantom surface by addition of a gel layer. What is immediately apparent is the much greater coherency between the responses measured at the different element positions. There are now perceivable gaps in the arrival times of the leading edge of the wavefront at the different element positions, with the wave first arriving at element position 16 and last at element 112 as expected. Although there is still some non-uniformity in the arrival time intervals, this is much more conceivably due to noise in the measurements rather than a fundamental issue with the method.

Unfortunately the arrival time intervals are still significantly shorter than expected using this technique. Using the cross-correlation technique described in section 3.3.1, an overall estimated wave speed of  $8.0 \text{ ms}^{-1}$  was found for displacement response that figure 3.8(b) was taken from, this to be compared with the expected shear wave velocity of  $2.89 \text{ ms}^{-1}$ . This suggests there is still some unaccounted for factor.

### 3.2.3 Effects of rigid boundaries of phantom

One aspect of the phantom which is clearly non-realistic is its cuboidal form and rigid casing. In-vivo tissue is generally much less strongly confined and hard surfaces the tissue is coupled to such as bones are relatively irregular in form. Intuitively it would seem both these factors will favour stronger and more frequent reflections in the phantom than would be evident in real tissue. As it has been suggested that the interference of such reflections with the original wave and other related effects may be the basis for some of the discrepancies observed in the results so far, further investigation of this issue was conducted.

A related theoretical discussion is presented in [17]. This argues that the usual distinction made between shear and compression waves is somewhat arbitrary, with in general waves able to continuously vary between exciting the medium they are travelling through perpendicularly to their direction of travel (the common definition of shear waves) and parallel to their direction of travel (the common definition of compressional waves). It is suggested a more appropriate distinction is between the irrotational wave component  $\nabla\phi$  and equivoluminal wave component  $\nabla \times \mathbf{p}$ , with a vector wave displacement field  $\mathbf{u}$  able

to be written as the sum of these two components

$$\mathbf{u} = \nabla\phi + \nabla \times \mathbf{p} \text{ or equivalently } u_i = \partial_i\phi + \epsilon_{ijk}\partial_j p_k$$

and each satisfying an independent reduced wave equation. What is commonly termed the shear wave speed  $c_s = \sqrt{\frac{\mu}{\rho}}$  is actually the speed of the wave solution of the equation satisfied by the equivoluminal wave component, and similarly the compressional wave speed  $c_c = \sqrt{\frac{\lambda+2\mu}{\rho}}$  corresponds to the speed of the wave solution of the irrotational component.

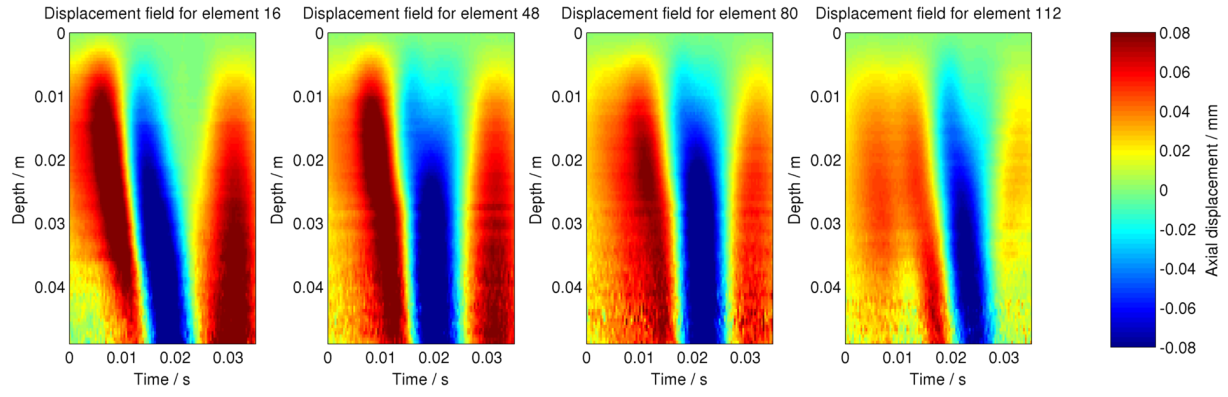
In [17] it is further demonstrated that the travel or phase speed of a wave is related to  $c_s$  and  $c_c$  in a complex manner which is dependent on the geometry of the wavefronts and medium being excited. In particular  $c_s$  only acts as a lower bound on the travel speed of shear waves, with equality occurring for uniform plane shear waves in an infinite medium.

As soft tissues are generally near incompressible, the irrotational component of the wave field in soft tissues is both very difficult to measure and contains little useful information about the tissue. The equivoluminal wave field component, which can be found from the curl of the displacement field, on the other hand allows determination of the shear wave speed and so with a constant density assumption, the shear modulus distribution.

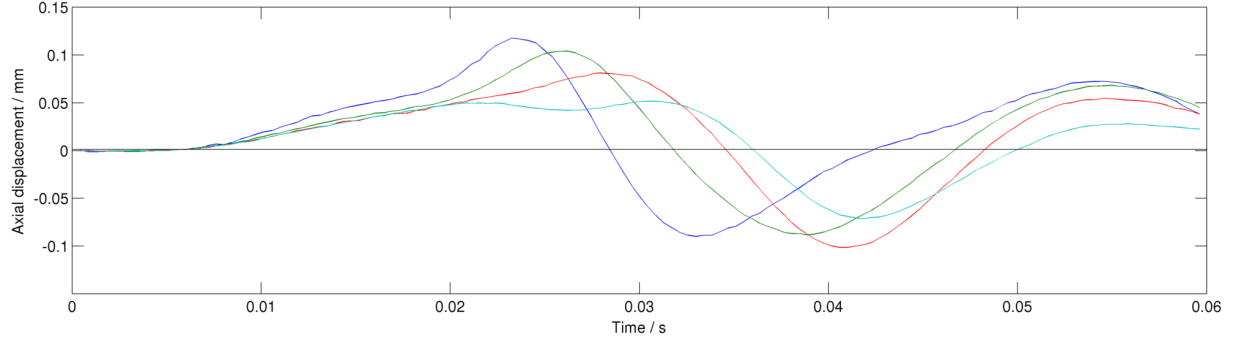
The use of ultrasound elastography techniques in this project, prevents the determination of the equivoluminal wave component as the curl operation requires the full vector displacement field to be known, which can only be determined currently with MRE or 3D ultrasound techniques. In acknowledgement of this inherent limitation the authors of [17] make a number of suggestions to maximise the validity of the assumption that shear waves will only propagate at a travel speed of  $c_s$ :

- minimising wave reflections by using a small excitation amplitude, this taking advantage of the damping nature of (in-vivo) soft tissue
- minimising the tissue excitation frequency to prevent creation of waves acting in higher modes and associated higher travel speeds, with a tradeoff in the associated decrease in damping
- using a tissue excitation method that produces wavefronts with a geometry close to the ideal of planar

This validates the conclusion reached above that minimising wave reflections might help to eliminate some of the discrepancies observed in the results. In order to provide some experimental results to test these ideas, it was decided to conduct a further set of phantom scans with the novel aspect of the probe being oriented at an angle to the phantom walls, all previous scans having been conducted with the lateral axis of the probe parallel to the walls of the phantom. The theory being tested was that this scan configuration would reduce any deleterious effect wave reflections off the phantom boundaries were having, as the reflections would now be less likely to directly return to the probe.



(a) Intervals of depth-time displacement profiles measured at different element positions



(b) Displacement responses measured at 2.5 cm depth

Figure 3.9: Examples of phantom scan results using angled probe orientation

This minor alteration resulted in a major improvement in the data recorded, with example plots for one of the sets of data recorded shown in figure 3.9. It can be seen that there is a clear and fairly uniform progression in the arrival time of corresponding points of the wave at the different element positions. Even more promising, the wave speeds predicted by the estimated arrival times agree much more closely with the expected result of  $2.89 \text{ ms}^{-1}$ , with the sample mean and standard deviation of the estimated wave speed (calculated as detailed in section 3.3.1) across five independent datasets being  $3.93 \text{ ms}^{-1}$  and  $0.25 \text{ ms}^{-1}$  respectively. This provides strong evidence that wave reflections in the phantom were negatively affecting the results.

### 3.3 Shear modulus estimation

Having now discussed the development of both the methods for measuring and exciting displacements in the tissue, the final area that needs to be covered is the investigations in to how the displacement data produced can be analysed to produce absolute shear modulus estimates.

### 3.3.1 Arrival time based methods

#### Cross-correlation based wave tracking

The method used to match sections of the displacement responses measured at the different element positions and so compute the arrival time intervals was cross-correlation maximisation. The cross-correlation was computed along the time axis of a reference interval of the depth-time response measured at element position 16 (i.e. closest to the tap) with a search time range of the displacement responses at each of the other element positions. The time offsets associated with the maxima of the resulting one-dimensional cross-correlation plots were taken as the best estimates for the arrival time intervals of the wave at the different element positions. From the known spatial separations of the element positions, the travel velocities of the wavefronts between the element positions were then estimated and then used to form estimates of the shear modulus using  $\mu = \rho_{\text{water}} c_s^2$ .

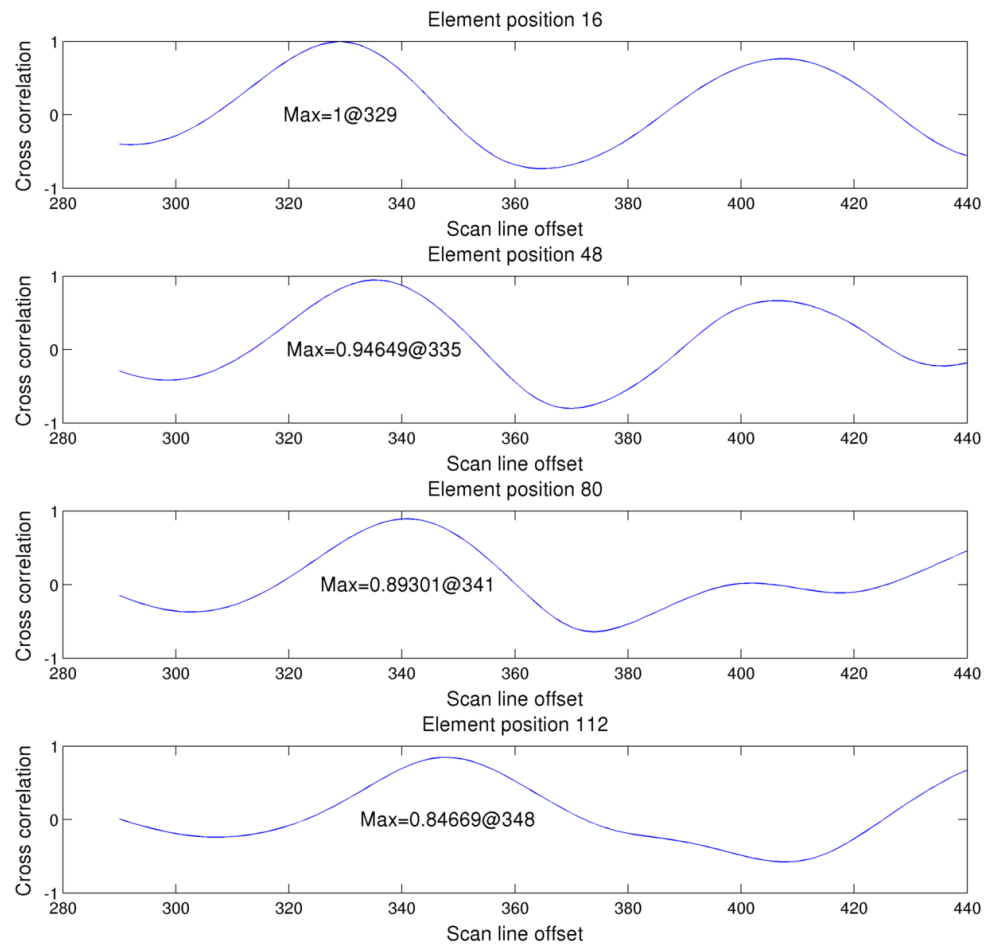


Figure 3.10: Example set of element position cross-correlation plots

Figure 3.10 shows a plot of the cross-correlations computed for one of the angled probe datasets discussed in section 3.2.3. The maximum peaks in the cross-correlation functions for the different elements are relatively evenly spaced with offsets corresponding to wave speeds of  $3.8 \text{ ms}^{-1}$ ,  $3.8 \text{ ms}^{-1}$  and  $3.2 \text{ ms}^{-1}$ . The cross-correlation search range for these

plots was widened to show the presence of further peaks at higher offsets, corresponding to matches of the reference patch with similar regions later on in the displacement responses. Although here the additional correlation peaks are lower than those at the ‘correct’ offsets, this will not always be the case, so in general the search range needs to be chosen carefully based on the expected time offsets to minimise the risk of false matches.

## Localisation

The basic wave tracking method just described, matches across the whole displacement response depth range at once and therefore does not give localisation of the shear modulus estimates axially. As an extension to this scheme, the data was windowed axially and then cross-correlation applied across the corresponding depth windows. As a further addition cubic splines were fitted to the windows of data and used to subsample the data along the time axis prior to cross-correlation computation to try to increase the precision of the shear modulus estimates.

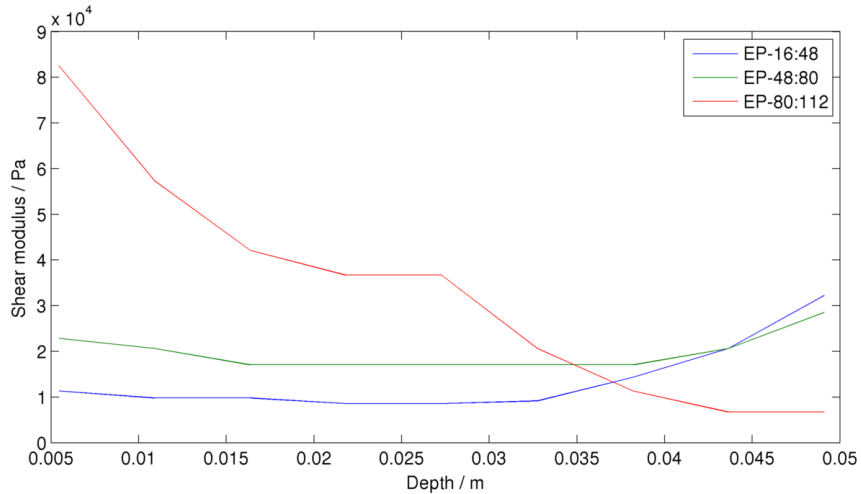


Figure 3.11: Example of localised shear modulus distribution estimate

An example plot of the estimated shear modulus distribution for this scheme is shown in figure 3.11. An axial window size of 9 samples was used, producing 11 windows in the axial direction for the data used. Prior to the computation of the shear moduli estimates a 3 element median filter was applied along the windowed scan line offset estimates for each of the element position pairs to try to remove false match outliers. The displacement responses were measured in a region of the phantom containing a type IV spherical inclusion of shear modulus  $26.7 \pm 2.7$  kPa against the background shear modulus of  $8.3 \pm 1.3$  kPa. Although the estimated shear modulus profiles are roughly of the overall correct scale, no useful localisation has been achieved with the stiffer spherical region not having being picked out at all and the results generally fairly poor. This was repeated across the other datasets tested suggesting the algorithm used here is not beneficial without further refinement over the whole depth correlation scheme explained above.

### 3.3.2 Direct inversion

#### Implementation of basic inversion algorithm

The first step taken in developing the inversion approach to shear modulus estimation, was implementing the basic technique presented in section 2.2. For the initial implementation basic second order finite difference approximations were used to calculate the displacement field derivatives.

A subtlety not highlighted in the SSI and PTE papers is that the inversion problem is ill-posed for displacement field regions where the spatial second derivative sum is zero. Any such points were therefore ignored when averaging the shear modulus estimates, with the normalisation factors for the averaging operation updated to reflect the fact that the summation is over a reduced set of estimates.

#### Verification with simulated data

To verify the basic inversion algorithm functioned in ideal circumstances, a set of synthetic displacement data simulating the pass of a planar shear wave across a region of uniform shear modulus and density containing a spherical inclusion of higher shear modulus was produced using the finite difference simulator.

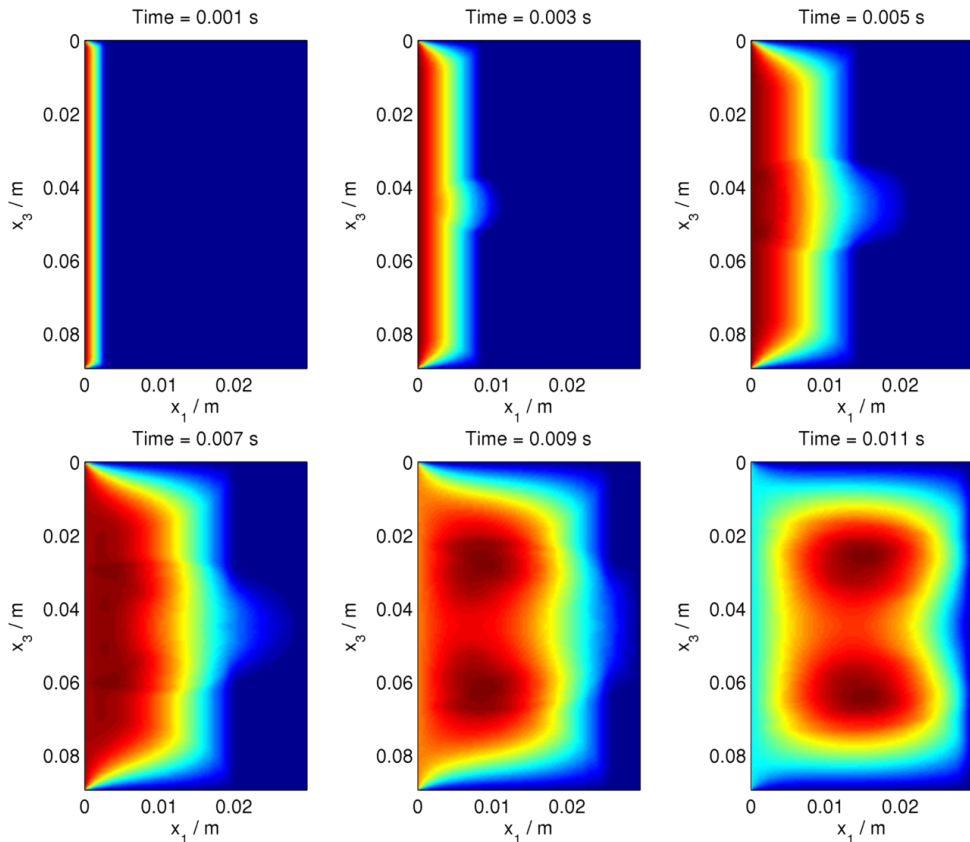


Figure 3.12: Simulated axial displacement fields for planar shear wave propagation across stiffer spherical inclusion

The shear wave was induced in the simulation by specifying a single period sinusoidal excitation of one face of the simulated region (normal to the lateral axis) in the axial direction. The boundaries normal to the axial direction were set to be rigidly constrained to model the confining effects of the probe and phantom casing. Figure 3.12 shows the simulated axial displacement field on a plane through the modelled region at six time steps.

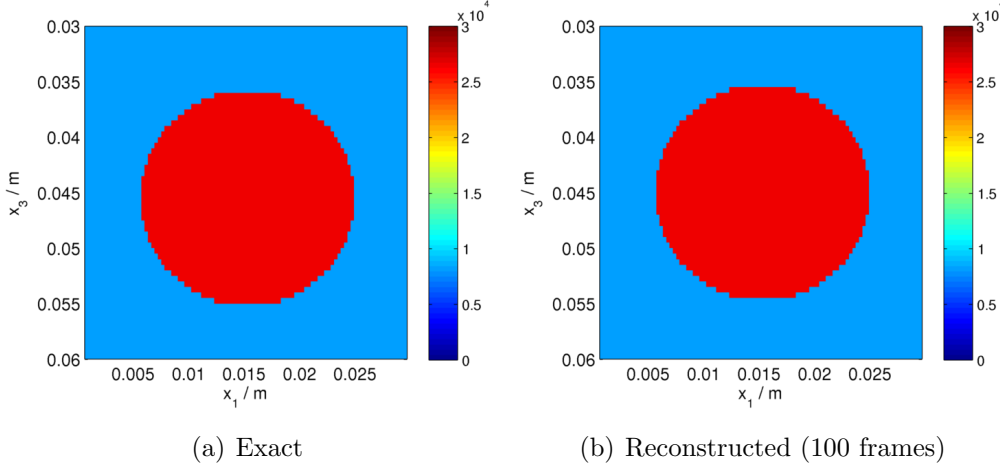


Figure 3.13: Exact and reconstructed shear modulus (Pa) images using direct inversion method on 100 timesteps of simulated data of plane shear wave in spherical phantom

The result of applying the inversion algorithm to the simulated dataset is shown in figure 3.13(b) alongside the actual shear modulus distribution 3.13(a). It can be seen that the shear modulus has been recovered exactly as would be expected. It does however verify that the inversion algorithm implementation works and in particular the method for dealing with the ill-posedness of the inversion problem functions correctly.

### Improving noise robustness

In general measured displacement fields will be subject to significant noise, in which case the high-frequency noise amplification effects of finite difference derivative estimations will wipe out any useful information in the recovered estimates. Techniques for providing robustness to noise in the inversion algorithm implementation will therefore be essential to providing useful results from real data.

Estimations of derivatives from finite sets of sampled, noisy, measured data is well studied and a variety of different schemes have been proposed. A commonly used approach in elastography applications, particularly MRE e.g. [13], is Savitzky-Golay filtering, which fits a polynomial to local windows of the data and approximates the local derivatives from the relevant polynomial coefficients [18]. By varying the window length and polynomial order differing levels of smoothing can be achieved. A more generic approach is to smooth with a Gaussian kernel prior to differentiation with standard finite difference operators.

There is also potential scope for improving noise robustness by using a different scheme for combining the shear modulus estimates computed for each spatial point across the measured time points. The *simple ratio averaging* (SRA) scheme used in the basic implementation is very susceptible to noise as low values of the denominator (spatial Laplacian approximation) will significantly amplify noise in the numerator (temporal second derivative approximation).

This observation suggests a simple scheme for increasing noise robustness is to apply a threshold to the absolute value of the estimated denominator terms and only average over the values where the threshold is exceeded. This scheme, which will be termed *thresholded ratio averaging* (TRA) has the disadvantages however of requiring selection of a suitable threshold value somehow and of biassing the results given denominator values which tend to give higher shear modulus estimates are being ignored.

In appendix B a more rigorous probabilistic approach to estimating a ratio from noisy measurements is used to derive a *noise robust ratio estimator* (NRRE) which it is shown in tests with synthetic data recovers ratios well even when there is severe noise present. This estimator assumes that the numerator and denominator terms are both subject to zero-mean Gaussian noise of fixed variances (at each point) and that the noise is uncorrelated with the underlying data, likely a simplification of the real nature of the noise present. Importantly it is allowed for the noise in the numerator and denominator terms to be correlated as the finite difference derivative approximations being used to calculate the denominator and numerator values all share the central displacement measurement in their computations and so would be expected to be correlated.

The NRRE scheme effectively weights each ratio value by the square of the denominator, thus favouring points where the denominator is high and so noise amplification is low. The estimates are then normalised by the sum of the individual denominator squares and terms involving the local noise parameters which adjust the estimate to remove multiplicative and additive bias introduced by the weighting and noise correlation respectively.

Several methods could be used to find suitable values for the local noise parameters. Various algorithms exist for estimating noise parameters by fitting a model to data. Alternatively the imaging system could be ‘calibrated’ by measuring the shear modulus distribution of a reference object and optimising the noise parameters to correct bias in the estimated distribution, subject to some form of regularisation to minimise over-fitting. For data with a reasonably high SNR, the affect of the noise parameters on the estimate is small and so using incorrect values is of little consequence, while this scheme still provides a distinct advantage over SRA which is sensitive to even small noise levels.

## Tests with simulated data

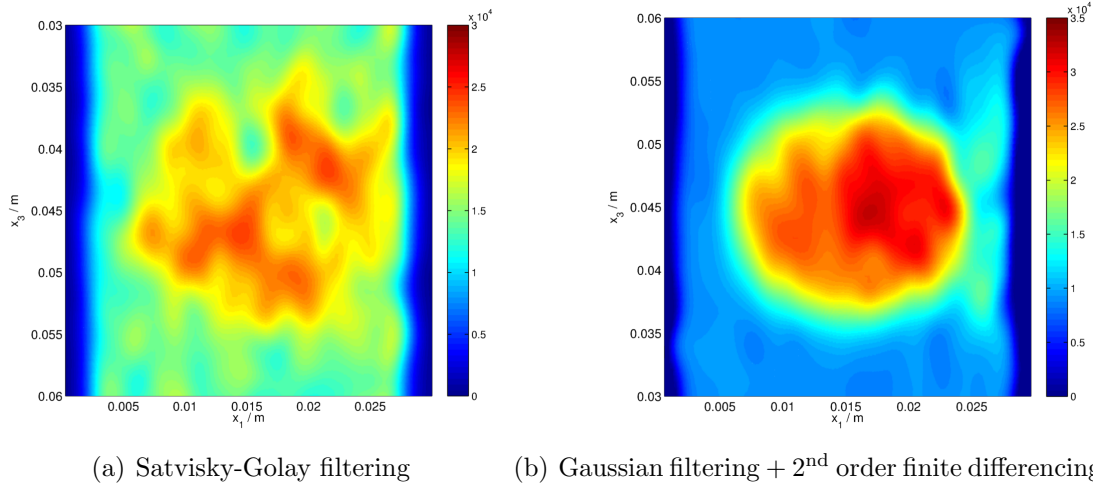


Figure 3.14: Reconstructed shear modulus (Pa) images from simulated data with additive noise comparing derivative approximation schemes (note different colour scales). In both cases the NRRE scheme was used to combine the data.

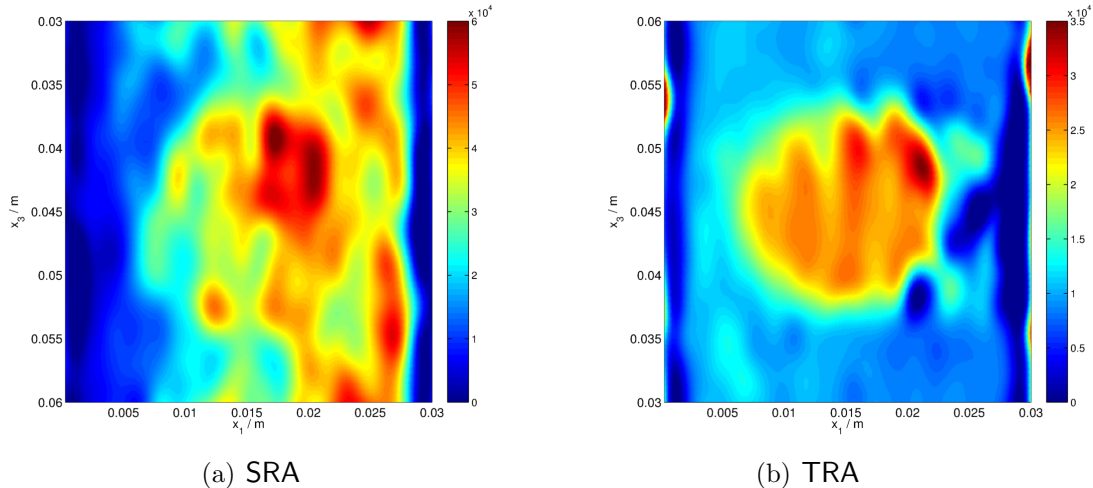


Figure 3.15: Reconstructed shear modulus (Pa) images from simulated data with additive noise comparing alternative ratio estimation schemes (note different colour scales). In both cases finite difference approximations with Gaussian filtering where used to compute the derivatives.

Figures 3.14 and 3.15 show reconstructed shear modulus distributions from the previously simulated plane shear wave displacement data with added Gaussian white noise simulating an SNR of around 10.

The plots in figure 3.14 show the reconstructions using the two derivative estimation schemes detailed above with 3.14(a) having been produced using Satvisky-Golay filtering (window length 17, polynomial order 2) and 3.14(b) produced by first filtering three-dimensionally with an isotropic Gaussian kernel (standard deviation 3) and then using

standard finite difference approximations. For both NRRE was used as the ratio estimation scheme, with the noise parameter terms neglected to allow the relative biases introduced by each of two derivative approximation schemes to be compared fairly.

It is clear that the Gaussian filtering method has performed significantly better than Savitzky-Golay filtering, with figure 3.14(b) showing much better recovery of the shape of the spherical inclusion and significantly better quantitative values for the shear modulus estimates in the two different regions other than a small over-bias in the background estimates.

Figure 3.15 shows the reconstructed shear modulus distributions when using SRA (figure 3.15(a)) and TRA (figure 3.15(b)) for the ratio estimation scheme. The other aspects of the inversion algorithm were identical to those used for figure 3.14(b) to allow for direct comparison with the performance of the NRRE scheme.

It is evident from 3.15(a) that the SRA scheme performs very poorly, with the spherical inclusion region not distinguishable from the background and much of the background region having its shear modulus significantly overestimated. The additional thresholding step in TRA gives a noticeable improvement, with the inclusion being easy to pick out in figure 3.15(b), however compared to 3.14(b) there is more bias to the shear modulus estimates in both regions and there is also more noise evident with the inclusion shape recovered less accurately. The threshold used for the TRA reconstruction was 1, which subjectively gave the best performance.

### Inversion from sparsely sampled displacement fields

All the tests of the inversion method that have been discussed so far have used the full displacement fields calculated by the simulator. This is not representative of the temporal and spatial density of data that will be available with the actual developed scanning method - in particular data will only be recorded at eight positions in the lateral direction and the temporal resolution will be significantly less than the simulation time step.

To test whether the developed inversion method could recover structure from more representative datasets, the data from the plane shear wave simulation used in the previous section was sub-sampled in the lateral and temporal dimensions to model the dataset that would be acquired by an eight element scan sequence scanning to a depth of 5 cm. This data, initially noiseless, was then inverted as previously, with Gaussian filtering (standard deviation 1) applied prior to the finite difference derivative calculations and the NRRE scheme used to combine the data.

The result for one lateral position is shown in 3.16(a). Even with this significantly reduced dataset the shear modulus distribution has still been recovered reasonably well, though some bias appears to have been introduced in the estimates.

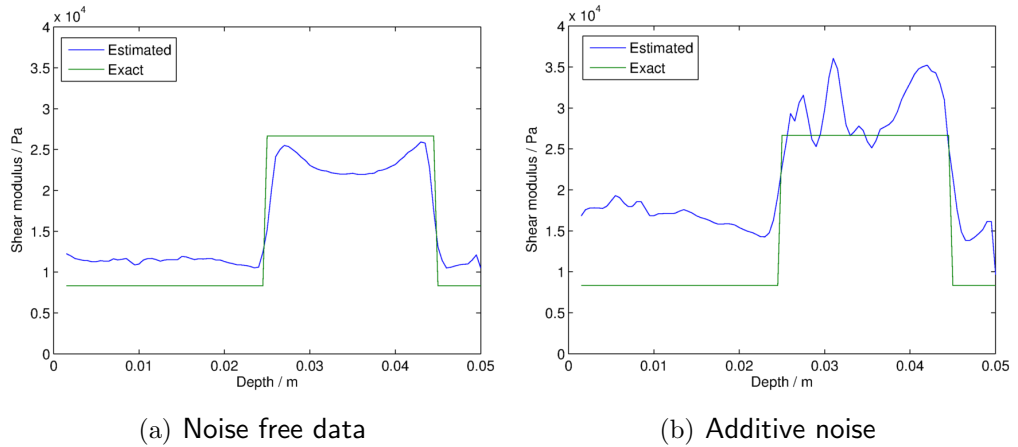


Figure 3.16: Reconstructed shear modulus plots along axial scan-line through centre of simulated spherical phantom from sparsely sampled sets of simulated data

It was found however the use of sparser datasets vastly increased the noise sensitivity of the developed technique. Figure 3.16(b) shows the recovered shear modulus profile after addition of Gaussian noise of standard deviation one-thousandth of the displacement data standard deviation. Even with this very low noise level the quality of the reconstruction has significantly reduced, with noise levels beyond this order of magnitude appearing to make the shear modulus unrecoverable from the data using the current method.

## 4. RESULTS AND DISCUSSION

Results for the stiffness estimates produced using the methods developed in the previous section will now be presented and briefly discussed to assess the overall performance of the developed schemes.

### 4.1 Tissue mimicking phantom scans

A set of scans of a region of the phantom containing the type IV large spherical inclusion were conducted, with probe lateral axis non-aligned with the phantom boundaries to minimise reflections as described in section 3.2.3. The probe was clamped in position over the scan region and an acoustic gel layer was used to provide acoustic coupling between the probe and phantom while minimising the effect of probe motion as described in section 3.2.2.

#### 4.1.1 Arrival time based shear modulus estimates

Given the localisation scheme did not appear to give any useful extra information, for the arrival time based results wave tracking was conducted by correlating displacement field intervals across the full depth range. Thus the results gained are an estimate of some measure of the overall scale of the shear modulus distribution in the region.

Dataset	1	2	3	4	5	Mean	Std. Dev.
Shear wave speed est. / $\text{ms}^{-1}$	4.01	4.26	3.59	3.78	4.01	3.93	0.25

Table 4.1: Shear wave speed estimates using arrival time method for phantom scans

The results shown in table 4.1 are the estimated shear wave speed in the scanned phantom region for five independent scan datasets. The mean corresponds to a shear modulus of 15.4 kPa which can be compared with the actual values of 8.3 kPa in the phantom background material and 26.7 kPa in the stiffer spherical inclusion. The arrival time method therefore seems to be producing reasonable results for the shear modulus under the scanning conditions used, although without localisation this single value is of limited use in meeting the original aim of providing a calibration point for a QUE image.

#### 4.1.2 Direct inversion based shear modulus estimates

Scans of the phantom were also conducted with the eight element scan sequence designed for recording data for use with the inversion scheme. Given the sensitivity to noise when using representatively sparse subsets of the simulated data shown in section 3.3.2, it did not seem likely the current method would produce particularly useful results with the inherently noisy measured data, and this was borne out in the results.

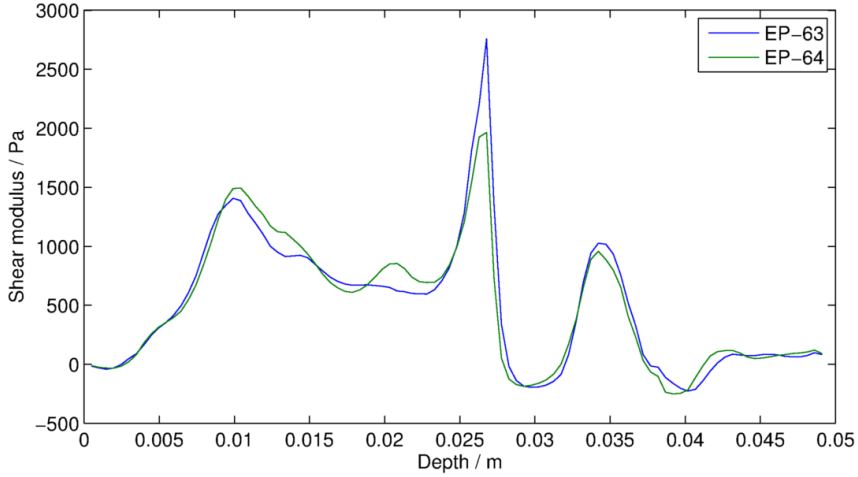


Figure 4.1: Example of estimated shear modulus profiles produced using inversion method on phantom scan data

Inversion was attempted with Gaussian filtering, finite difference derivative approximations and the NRRE scheme for combining the data as this was the combination which performed best with the noisy simulated data. Even with very severe low-pass Gaussian filtering the results produced showed very little structure and in overall scale were very significantly different from the expected values. An example of a shear modulus estimate profile produced is shown in figure 4.1. This suggests the inversion scheme as currently implemented is not suitable for use with such sparse datasets.

## 4.2 In-vivo calf muscle scans

To provide a small test of how well the developed method might work in a more clinically realistic situation, a set of scans of a region of in-vivo tissue were recorded. In particular a region of calf muscle was scanned using the four-element wave tracking based scan sequence and a tap applied to the tissue at around a distance of 5 cm from the probe. In this case it was not possible to clamp the probe in position and water rather than acoustic gel was used to acoustically couple the probe to the tissue surface.

An example set of displacement time profiles are shown in figure 4.2. Although there is clearly more noise present in the data than the phantom scans as would be expected from the less controlled conditions, the overall pattern observed seems to be similar, with what appears to be shear wavefronts moving across the element positions. Note the line / block artefacts evident in these plots are the result of the use of Stradwin's 2D tracking capability (rather than the axial only tracking used in the previous results) which is applied separately to each 'frame' of 128 scan-lines and so results in small discontinuities at the frame boundaries. This was necessary to overcome problems with the tracking algorithm failing when restricted to one dimensional only searches.

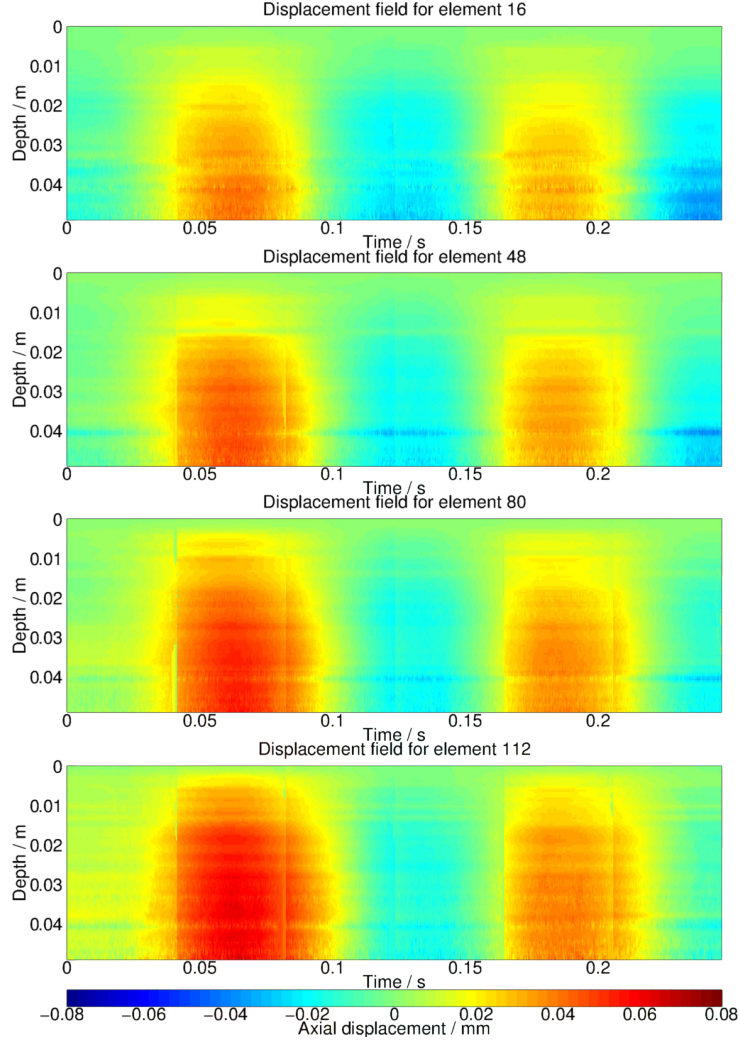


Figure 4.2: Axial displacement responses measured at different element positions to tap in region of in-vivo calf tissue

Dataset	1	2	3	Mean	Std. Dev.
Shear wave speed estimate / $\text{ms}^{-1}$	2.63	6.02	2.14	3.6	2.1

Table 4.2: Shear wave speed estimates using arrival time method for calf muscle scans

Table 4.2 shows the shear wave speeds estimated from three sets of scan data. In [19] a typical shear modulus for calf muscle is given as  $5.1 \pm 0.9 \text{ kPa}$  corresponding to a shear wave speed of  $2.3 \pm 0.2 \text{ ms}^{-1}$ . Although clearly the measured values have significant variance, they seem to be plausibly close to this value. Significantly, despite the much more noisy data, the estimated wave speeds are much closer to expected value than was the case for the initial phantom tests which were out by around a factor of 4 (prior to the use of a non-aligned configuration) providing further evidence that the rigid boundaries of the phantom and the resulting strong reflections may have been the cause of some of the discrepancies observed.

## 5. CONCLUSIONS

From the results just presented it is evident that the original objective of producing a complete method of estimating absolute tissue stiffness at a small set of points using only conventional ultrasound hardware has not been achieved. Although significant work has been done in developing the proposed method, the results obtainable at the moment with measured as opposed to simulated data are lacking in several important respects.

For the arrival time method, although plausible shear modulus values were obtained in both scans of a tissue mimicking phantom and an in-vivo region of human calf tissue, importantly no localisation of these estimates was achieved. This precludes the method of using absolute point measurements to calibrate a relative stiffness image produced using QUE as originally proposed. However assuming the measured value represents the average shear modulus across a region, the average of the relative stiffness values of a QUE image could conceivably be matched to this value to provide a coarse calibration.

Although some basic attempts at localising the data were discussed, the cross-correlation displacement field window matching method developed did not seem to give any useful results. As the issues encountered with probe motion and wave reflections took a significant time to resolve, only a limited amount of time was spent developing and investigating improvements to the localisation scheme so it seems likely there are grounds for improvement there, for example in using alternative window matching metrics such as phase correlation.

In the case of the inversion based method, it is less clear how much more scope for improvement there is on the already developed method. It seems that the combination of the sparsity of the displacement measurements that can be acquired with a conventional ultrasound scanner and the fact that real measurements will be subject to at least some noise may be a fundamental barrier to a successful implementation. Although refinements were made to the basic inversion scheme making it robust to significant noise levels in a spatially and temporally dense set of simulated displacements, when datasets more representative of that obtainable with an ultrasound imaging system were used, even very small noise levels significantly degraded the results.

It should also be reiterated that although the original PTE and SSI papers presented the direct inversion algorithm as the method used to form stiffness images from the measured displacements, later papers suggest arrival time techniques are instead being used, and so it is not clear if the inversion method is actually being used with these approaches in practice.

One potential area of improvement in the current implementation of the inversion scheme, would be to use a maximum-a-posteriori ratio estimator scheme as opposed to the maximum likelihood estimator developed here. Use of appropriate (probably neces-

sarily conjugate) priors might help to counteract the problems encountered because of the sparseness of the data.

The quality values associated with each displacement estimate (from the window matching scheme being used) were not exploited at all in this work, and could also potentially be a source of improvements. For instance they could be used to adaptively filter the displacement field prior to derivative approximation based on the estimated local displacement qualities, and/or used as a measure of the local noisiness of the data in the ratio estimation scheme.

## BIBLIOGRAPHY

- [1] J. Ophir, I. Céspedes, H. Ponnekanti, Y. Yazdi, and X. Li. Elastography: A quantitative method for imaging the elasticity of biological tissues. *Ultrasonic Imaging*, 13(2):111 – 134, 1991.
- [2] J Foucher, E Chanteloup, J Vergniol, L Castéra, B Le Bail, X Adhoute, J Bertet, P Couzigou, and V de Lédinghen. Diagnosis of cirrhosis by transient elastography (fibroscan): a prospective study. *Gut*, 55(3):403–408, 2006.
- [3] J. Greenleaf, M. Fatemi, and M. Insana. Selected methods for imaging elastic properties of biological tissues. *Annual Review of Biomedical Engineering*, 5(1):57–78, 2003.
- [4] Joseph Schmitt. Oct elastography: imaging microscopic deformation and strain of tissue. *Opt. Express*, 3(6):199–211, Sep 1998.
- [5] Armen Sarvazyan. Mechanical imaging:: A new technology for medical diagnostics. *International Journal of Medical Informatics*, 49(2):195 – 216, 1998.
- [6] Peter N. T. Wells and Hai-Dong Liang. Medical ultrasound: imaging of soft tissue strain and elasticity. *Journal of The Royal Society Interface*, 2011.
- [7] G. Treece, J. Lindop, L. Chen, J. Housden, R. Prager, and A. Gee. Real-time quasi-static ultrasound elastography. *Interface Focus*, 1(4):540–552, 2011.
- [8] L. Sandrin, M. Tanter, S. Catheline, and M. Fink. Shear modulus imaging with 2-d transient elastography. *Ultrasonics, Ferroelectrics and Frequency Control, IEEE Transactions on*, 49(4):426 –435, April 2002.
- [9] J. Bercoff, M. Tanter, and M. Fink. Supersonic shear imaging: a new technique for soft tissue elasticity mapping. *Ultrasonics, Ferroelectrics and Frequency Control, IEEE Transactions on*, 51(4):396 –409, April 2004.
- [10] L. Sandrin, S. Catheline, M. Tanter, and X. Hennequin. Time-resolved pulsed elastography with ultrafast ultrasonic imaging. *Ultrasonic imaging*, 21(4):259–272, December 1999.
- [11] Lin Ji, Joyce R McLaughlin, Daniel Renzi, and Jeong-Rock Yoon. Interior elastodynamics inverse problems: shear wave speed reconstruction in transient elastography. *Inverse Problems*, 19(6):S1, 2003.
- [12] J. McLaughlin and D. Renzi. Shear wave speed recovery in transient elastography and supersonic imaging using propagating fronts. *Inverse Problems*, 22(2):681, 2006.
- [13] T. Oliphant, A. Manduca, R. Ehman, and J. Greenleaf. Complex-valued stiffness reconstruction for magnetic resonance elastography by algebraic inversion of the differential equation. *Magnetic Resonance in Medicine*, 45(2):299–310, 2001.
- [14] J. Ophir, Sk Alam, B. Garra, F. Kallel, C. R. B. Merritt, R. Righetti, R. Souchon, S. Srinivasan, and T. Varghese. Elastography: Imaging the Elastic Properties of Soft Tissues with Ultrasound. *Journal of Medical Ultrasonics*, 29:155–171, December 2002.
- [15] O. S. Boyd. An efficient Matlab script to calculate heterogeneous anisotropically elastic wave propagation in three dimensions. *Computers and Geosciences*, 32:259–264, March 2006.
- [16] J. E. Lindop, G. M. Treece, A. H. Gee, and R. W. Prager. Phase-based ultrasonic deformation estimation. Technical report, IEEE Transactions on Ultrasonics, Ferroelectrics, and Frequency Control, 2006.
- [17] Ali Baghani, Septimiu Salcudean, and Robert Rohling. Theoretical limitations of the elastic wave equation inversion for tissue elastography. *The Journal of the Acoustical Society of America*, 126(3):1541–1551, 2009.
- [18] Abraham. Savitzky and M. J. E. Golay. Smoothing and differentiation of data by simplified least squares procedures. *Analytical Chemistry*, 36(8):1627–1639, 1964.
- [19] M. Suga, T. Matsuda, K. Minato, O. Oshiro, K. Chihara, J. Okamoto, O. Takizawa, M. Komori, and T. Takahashi. Measurement of in vivo local shear modulus using mr elastography multiple-phase patchwork offsets. *Biomedical Engineering, IEEE Transactions on*, 50(7):908 –915, July 2003.

## A. RISK ASSESSMENT EVALUATION

This project lacked major hazards and this was reflected in the initial risk assessment. The main risks identified were ergonomic issues related to improper posture and workstation set-up when using computing equipment and delivery of excessive levels of acoustic ‘radiation’ when conducting in-vivo scans.

The former of these was a risk of relatively high occurrence probability but low potential for harm, with a low risk overall. The standard suggested mitigation techniques were generally observed and no ill effects as a result of project related computer use were observed over the course of the project.

The latter risk was much more project specific. As most scans were conducted on a phantom there was a low exposure to this risk overall. The scans which were conducted on a human subject were performed by and on an ultrasound imaging expert. Scans were kept to a minimal duration and the ultrasound system used has a very low power output, in particular being unable to produce ultrasound beams of sufficient intensity to produce the ‘push pulses’ seen in ARFI imaging.

## B. NOISE ROBUST RATIO ESTIMATOR DERIVATION

It is wished to estimate  $R = \frac{y_i}{x_i}$  given noisy measurements  $\tilde{x}_i = x_i + v_i$  and  $\tilde{y}_i = y_i + w_i \forall i \in \{1 \dots N\}$ . Define

$$\mathbf{x} = [x_1 \ x_2 \ \dots \ x_N]^T \quad \mathbf{v} = [v_1 \ v_2 \ \dots \ v_N]^T \quad \tilde{\mathbf{x}} = \mathbf{x} + \mathbf{v} = [\tilde{x}_1 \ \tilde{x}_2 \ \dots \ \tilde{x}_N]^T$$

$$\mathbf{y} = [y_1 \ y_2 \ \dots \ y_N]^T \quad \mathbf{w} = [w_1 \ w_2 \ \dots \ w_N]^T \quad \tilde{\mathbf{y}} = \mathbf{y} + \mathbf{w} = [\tilde{y}_1 \ \tilde{y}_2 \ \dots \ \tilde{y}_N]^T$$

Assume  $\mathbf{v}$  and  $\mathbf{w}$  are correlated Gaussian white noise vectors with known variances  $\sigma_v$  and  $\sigma_w$  respectively and correlation coefficient  $\varrho$

$$\begin{bmatrix} \mathbf{v} \\ \mathbf{w} \end{bmatrix} \sim \mathcal{N}\left(\begin{bmatrix} \mathbf{0} \\ \mathbf{0} \end{bmatrix}, \begin{bmatrix} \sigma_v^2 \mathbf{I} & \varrho \sigma_v \sigma_w \mathbf{I} \\ \varrho \sigma_u \sigma_v \mathbf{I} & \sigma_w^2 \mathbf{I} \end{bmatrix}\right)$$

$\Rightarrow \tilde{\mathbf{x}}$  and  $\tilde{\mathbf{y}}$  are jointly Gaussian distributed as well

$$\begin{bmatrix} \tilde{\mathbf{x}} \\ \tilde{\mathbf{y}} \end{bmatrix} \sim \mathcal{N}\left(\begin{bmatrix} \mathbf{x} \\ R\mathbf{x} \end{bmatrix}, \begin{bmatrix} \sigma_v^2 \mathbf{I} & \varrho \sigma_v \sigma_w \mathbf{I} \\ \varrho \sigma_v \sigma_w \mathbf{I} & \sigma_w^2 \mathbf{I} \end{bmatrix}\right)$$

Using standard results for the marginalisation of a joint Gaussian distribution, the conditional distribution of  $\tilde{\mathbf{y}}$  on  $\tilde{\mathbf{x}}$  is

$$\tilde{\mathbf{y}}|\tilde{\mathbf{x}} \sim \mathcal{N}(\boldsymbol{\mu}_{\tilde{\mathbf{y}}|\tilde{\mathbf{x}}}, \boldsymbol{\Sigma}_{\tilde{\mathbf{y}}|\tilde{\mathbf{x}}}) \text{ with } \boldsymbol{\mu}_{\tilde{\mathbf{y}}|\tilde{\mathbf{x}}} = R\mathbf{x} + \frac{\varrho \sigma_w}{\sigma_v}(\tilde{\mathbf{x}} - \mathbf{x}) \text{ and } \boldsymbol{\Sigma}_{\tilde{\mathbf{y}}|\tilde{\mathbf{x}}} = \sigma_v^2(1 - \varrho^2)\mathbf{I}$$

Let  $\mathcal{L}$  denote the natural logarithm of the conditional distribution  $p[\tilde{\mathbf{y}}|\tilde{\mathbf{x}}]$

$$\mathcal{L} = \ln(p[\tilde{\mathbf{y}}|\tilde{\mathbf{x}}]) = -\frac{N}{2} \ln(2\pi) - \frac{1}{2} \ln |\boldsymbol{\Sigma}_{\tilde{\mathbf{y}}|\tilde{\mathbf{x}}}| - \frac{1}{2} (\tilde{\mathbf{y}} - \boldsymbol{\mu}_{\tilde{\mathbf{y}}|\tilde{\mathbf{x}}})^T \boldsymbol{\Sigma}_{\tilde{\mathbf{y}}|\tilde{\mathbf{x}}}^{-1} (\tilde{\mathbf{y}} - \boldsymbol{\mu}_{\tilde{\mathbf{y}}|\tilde{\mathbf{x}}})$$

Conditional distribution  $p[\tilde{\mathbf{y}}|\tilde{\mathbf{x}}]$  is maximised with respect to  $R$  when  $\frac{d\mathcal{L}}{dR} = 0$

$$\Rightarrow \frac{d\mathcal{L}}{dR} = \frac{1}{\sigma_w^2(1 - \varrho^2)} \left( \tilde{\mathbf{y}}^T \mathbf{x} - R \mathbf{x}^T \mathbf{x} - \frac{\varrho \sigma_w}{\sigma_v} \mathbf{x}^T (\tilde{\mathbf{x}} - \mathbf{x}) \right) = 0$$

The estimator  $\hat{R}$  which maximises  $p[\tilde{\mathbf{y}}|\tilde{\mathbf{x}}]$  is therefore

$$\hat{R} = \frac{\tilde{\mathbf{y}}^T \mathbf{x} - \frac{\varrho \sigma_w}{\sigma_v} (\mathbf{x}^T \tilde{\mathbf{x}} - \mathbf{x}^T \mathbf{x})}{\mathbf{x}^T \mathbf{x}}$$

This involves terms in the unknowns  $\mathbf{x}$  and  $\mathbf{y}$  therefore approximations of these terms are needed.

$$\tilde{\mathbf{y}}^T \tilde{\mathbf{x}} = \tilde{\mathbf{y}}^T \mathbf{x} + \tilde{\mathbf{y}}^T \mathbf{v} = \tilde{\mathbf{y}}^T \mathbf{x} + R \mathbf{x}^T \mathbf{v} + \mathbf{w}^T \mathbf{v}$$

Assume  $\mathbf{x}$  and  $\mathbf{v}$  are uncorrelated and that  $N$  is sufficiently large that the finite summations in the vector scalar products can be approximated as expectations.

$$\Rightarrow \mathbf{x}^T \mathbf{v} = \sum_{i=1}^N (x_i v_i) \approx N E[x_i v_i] = 0 \quad \text{and} \quad \mathbf{w}^T \mathbf{v} = \sum_{i=1}^N (w_i v_i) N E[w_i v_i] = N \varrho \sigma_v \sigma_w$$

$$\therefore \tilde{\mathbf{y}}^T \mathbf{x} \approx \tilde{\mathbf{y}}^T \tilde{\mathbf{x}} - N \varrho \sigma_v \sigma_w$$

Using the same assumptions

$$\mathbf{x}^T \tilde{\mathbf{x}} = \mathbf{x}^T \mathbf{x} + \mathbf{x}^T \mathbf{v} \approx \mathbf{x}^T \mathbf{x}$$

and

$$\tilde{\mathbf{x}}^T \tilde{\mathbf{x}} = \mathbf{x}^T \mathbf{x} + 2\mathbf{x}^T \mathbf{v} + \mathbf{v}^T \mathbf{v} \approx \mathbf{x}^T \mathbf{x} + N\sigma_v^2 \Rightarrow \mathbf{x}^T \mathbf{x} \approx \tilde{\mathbf{x}}^T \tilde{\mathbf{x}} - N\sigma_v^2$$

Substituting these terms into to the expression for  $\hat{R}$  gives the approximated estimator  $\tilde{R}$  in terms of only the measured data  $\tilde{\mathbf{x}}$  and  $\tilde{\mathbf{y}}$  and assumed known or estimated noise parameters  $\varrho$ ,  $\sigma_v$  and  $\sigma_w$

$$\hat{R} \approx \tilde{R} = \frac{(\tilde{\mathbf{y}}^T \tilde{\mathbf{x}} - N\varrho\sigma_v\sigma_w) - \frac{\varrho\sigma_w}{\sigma_v}(\mathbf{x}^T \mathbf{x} - \mathbf{x}^T \mathbf{x})}{\tilde{\mathbf{x}}^T \tilde{\mathbf{x}} - N\sigma_v^2} = \frac{\tilde{\mathbf{y}}^T \tilde{\mathbf{x}} - N\varrho\sigma_v\sigma_w}{\tilde{\mathbf{x}}^T \tilde{\mathbf{x}} - N\sigma_v^2}$$

Figure B.1 shows the performance of this estimator for a synthetic dataset across a range of ratio values  $-10 \leq R \leq 10$ . Also shown are the estimates produced by simply forming an average of the ratio of the noisy measurements and averaging all ratios when the denominator is above a threshold (0.05 here).

The denominator vector  $\mathbf{x}$ , of length  $N = 500$ , was drawn from a zero-mean Gaussian distribution with standard-deviation 2 and the numerator vector calculated as  $\mathbf{y} = R\mathbf{x}$ . The noisy measured vectors  $\tilde{\mathbf{x}}$  and  $\tilde{\mathbf{y}}$  were formed by adding correlated white noise with  $\varrho = 0.5$ ,  $\sigma_v = 1$   $\sigma_w = 1$ . It is evident that even with this high noise data the robust scheme just derived has generally estimated the true value well and appears to be unbiased. In comparison the simple averaging scheme gives effectively useless results with any underlying signal wiped out by noise (note the vertical axis scale for this case) and the thresholded scheme gives poorer noise reduction and creates biased estimates.

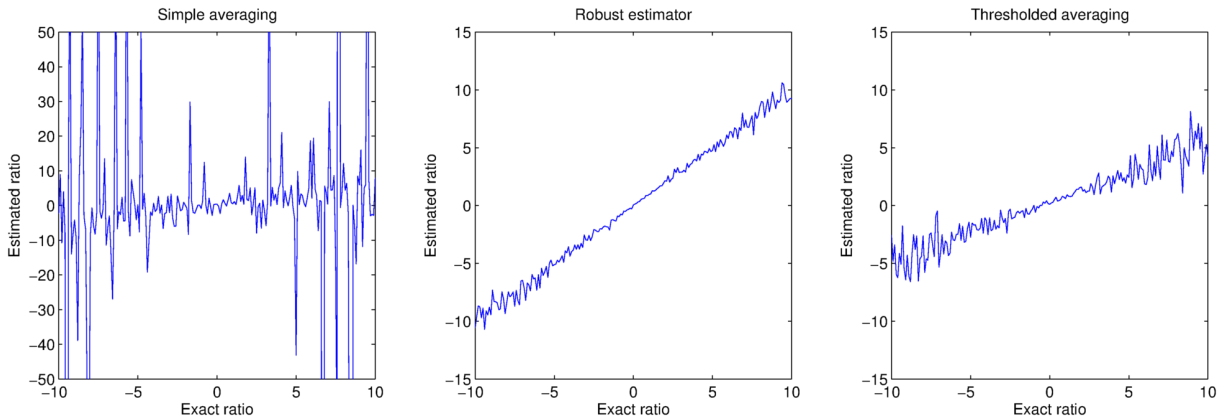


Figure B.1: Plots showing performance of different ratio estimation schemes